Diagnostics and Exploration of Current Sheet Formation in the High-Pulse-Rate Pulsed Inductive Thruster (HiPeR-PIT)

Cameron Marsh

A thesis
submitted in partial fulfillment of the
requirements for the degree of

Master of Science in Aeronautics and Astronautics

University of Washington

2022

Reading Committee:

Justin Little, Chair

Uri Shumlak

Program Authorized to Offer Degree:
College of Engineering,
William E. Boeing Department of Aeronautics and Astronautics

University of Washington

Abstract

Diagnostics and Exploration of Current Sheet Formation in the High-Pulse-Rate Pulsed Inductive Thruster (HiPeR-PIT)

Cameron Marsh

Chair of the Supervisory Committee:
Assistant Professor Justin Little
Aeronautics and Astronautics

Experimental measurements and numerical modeling of plasma current sheets in a new design for an Inductive Pulsed Plasma Thruster (IPPT) are presented. The High-Pulse-Rate Pulsed Inductive Thruster (HiPeR-PIT), is a low energy (∼3.8 J), planar coil, electrical propulsion concept employing a two-turn Archimedes spiral acceleration coil, and two stages of propellant pre-ionization, RF plasma discharge for the first stage, and a high frequency energy pulse through the acceleration coil for the second. Current sheet parameters were measured through the use of optical diagnostics and through an Electric field probe, B-dot probe, and Rogowski coil. Current sheet visualization from the optical diagnostics provided an estimated peak sheet velocity of ∼25 km/s. Several studies were performed to identify the ideal operating conditions of the thruster by varying the voltage of the main bank, varying the capacitance of the main bank, and varying the background gas pressure. Experimental results were compared to a one-dimensional numerical model. Results of the experiment matched the general trends from the numerical model initially, but diverged from the model in later simulation times. Results from both the numerical and experimental studies indicated potential advancement paths for the development of the HiPeR-PIT. Future improvements include increasing the chamber background pressure, increasing the energy per pulse, and adjusting the pre-ionization scheme to ensure uniform distribution of the pre-ionized gas.

TABLE OF CONTENTS

Page

LIST OF FIGURES

LIST OF TABLES

Table Number Page

Nomenclature

A_c	Coil cross sectional area (m^2)
A_s	Current sheet area (m^2)
B	Magnetic field ***vector***, scalar (T)
C	Capacitance (F)
D_p	Ambipolar plasma diffusivity coefficient (m^2/s)
E	Electric field ***vector***, scalar (V/m)
E_{pi}	Energy of pre-ionized plasma (J)
E_{tot}	Single pulse total energy (J)
H	Heaviside step function
I_c	Coil current (A)
I_p	Plasma current (A)
I_{bit}	Impulse bit ($N \cdot s$)
I_{sp}	Specific impulse (s)
J, j	Current density ***vector***, scalar (A/m^2)
L	Inductance (H)

L_0	Stray inductance (H)
L_c	Circuit inductance (H)
L_{eff}	Circuit effective inductance (H)
M	Mutual inductance (H)
P_{ei}	Power transferred from electron-ion Coulomb collisions (eV/s)
P_{en}	Power lost through inelastic collisions (eV/s)
P_{ohm}	Power gained from Ohmic heating (eV/s)
R_c	Circuit Resistance (Ω)
R_p	Plasma Resistance (Ω)
S_{es}	Polarization scattering reaction rate (m^3/s)
$S_{ex,j}$	Electron-impact excitation reaction rate (m^3/s)
S_{ion}	Electron-impact ionization reaction rate (m^3/s)
T_e	Electron Temperature (eV)
T_i	Ion Temperature (eV)
V	Voltage (V)
V_{ind}	Induced voltage (V)
W_a	atomic weight (amu)

$c_{s,f}$	Fast-moving neutral sound speed (m/s)
$c_{s,n}$	Slow-moving neutral sound speed (m/s)
d	Distance between electrode positions (m)
e	Electron elementary charge (C)
f_c	Collisional forces per unit atomic mass on plasma (s^{-2})
g_0	Gravitational Acceleration (m/s^2)
k	Coupling Coefficient
k_b	Boltzmann's constant (J/K)
m_e	Electron mass (kg)
m_i	Ion mass (kg)
m_{bit}	Mass bit (kg)
n_f	Fast-neutral number density (m^{-3})
n_n	Neutral number density (m^{-3})
n_s	Plasma number density (m^{-3})
r_i	Coil inner radius(m)
r_o	Coil outer radius(m)
t	Time (s)

v_s	Plasma sheet velocity (m/s)
$v_s f$	Difference of current sheet and fast neutral velocities (m/s)
w_s	Plasma sheet width (m)
z_a	Coil offset from gas injection (m)
z_c	Mutual decoupling length (m)
z_s	Plasma sheet position (m)
ΔV	Difference in Potential (V)
β_b	B-dot probe sensitivity factor (T/V)
β_r	Rogowski coil sensitivity factor (A/V)
χ_i	Pre-ionization fraction (s^{-1})
δ_s	Plasma skin depth (m)
ε_{ion}	Ionization energy for first ionization (eV)
ε^*_{ion}	Effective ionization energy (eV)
η_p	Plasma resistivity ($\Omega \cdot m$)
η_e	Electrical efficiency
η_m	Propellant mass utilization efficiency
η_T	Thrust efficiency

λ_f	Fast neutral sound speed (m/s)
$ln(\Lambda)$	Coulomb logarithm (m/s)
μ_0	Vacuum permeability (N/A^2)
ν_{ei}	Electron-ion Coulomb collision frequency (s^{-1})
ν_{en}	Electron-neutral Coulomb collision frequency (s^{-1})
ω	Plasma frequency (Hz)
σ_{cx}	Charge-exchange cross section (m^2)
σ_{en}	Electron-neutral collisional cross section (m^2)
$\Theta_{m,cx}$	Charge-exchange mass transparency current sheet
Θ_e	Electromagnetic transparency of current sheet
$\Theta_{m,ion}$	Ionization mass transparency of current sheet

ACKNOWLEDGMENTS

Several individuals have inspired and supported me throughout my time in the UW AA Master's program. I would like to acknowledge Professor Justin Little for accepting me into the UW SPACE lab and guiding me in this research. Your mentorship and enthusiasm in teaching plasmas has been an inspiration and continues to inspire my interests in plasma physics and electrical propulsion.

I would also like to thank Curtis, Gordon, and Arvindh of the PIT crew for their help and friendship during the HiPeR-PIT development and experiments. The countless days of experimentation were fun and engaging and I learned so much about IPPTs from all of you during those times.

I send thanks to all the members of the SPACE lab and the graduate office that I had the pleasure of socializing with on a daily basis, Peter, Sari, Isabella, Landon, Reed, Bennett, Jared, and Anna. Our study sessions improved my understanding of plasma physics in a way that I would not have accomplished alone.

Thank you to all of the teachers that have pushed me to succeed throughout my life. From my time in the Clark county school system, to the University of Nevada Las Vegas, and finally here at the University of Washington. Thank you to Professor Uri Shumlak, the quite literal other half of the UW AA plasma program who taught me so much about the fusion applications of plasma physics.

Thank you to Carter of the AA department facilities for your support throughout my teaching assistant-ships

Finally thank you to my family and friends outside of UW. Thank you to my parents Kimberly, William, and Mary for always supporting curiosity and creativity growing up.

DEDICATION

To my parents Kimberly, William, and Mary. Thank you for your unconditional love and support, pushing me to achieve my dreams.

Chapter 1

INTRODUCTION

Electrical propulsion (EP) has become one of the main-stays of propulsion sources in space in recent history particularly in orbital station-keeping applications. Electrical propulsion excels at low thrust applications such as station-keeping due the ability to precisely apply minute amounts of thrust efficiently. Particles in EP thrusters are often accelerated to high velocities on the order of 10,000 km/s. These high exhaust speeds allow many EP devices to operate with specific impulses above 1000 s, often an order of magnitude higher than chemical propulsion. This leads to larger mass utilization efficiencies compared to chemical propulsion which allows for less fuel mass onboard at the cost of increased power plant capacity and mass requirements. However, the low thrust capabilities of EP devices, which is in the range of Newtons, mean that takeoff from planetary surfaces will never be achieved without the help of higher power density engines. Due to these lower thrust capabilities, changes in speed take much longer than traditional propulsion methods, but the lifetime and fuel efficiency advantages allow for EP devices to accelerate aircraft to speeds far greater than chemical propulsion bringing into question replacement for in-space interplanetary missions. The advantages of using electrical propulsion is clear with superior lifetimes, fuel savings, and efficiency over traditional chemical thrusters. The focus of this thesis will be on the Inductive Pulsed Plasma Thruster, a device with sparse literature compared to many other types of electrical propulsion.

The Inductive Pulsed Plasma Thruster (IPPT) is an electric propulsion device which takes advantage of an inductive coil to ionize gas across its face from energy stored in a capacitor bank. The ionized gas then forms into a plasma current sheet opposing the current and magnetic field of the coil which creates a Lorentz body force between the coil

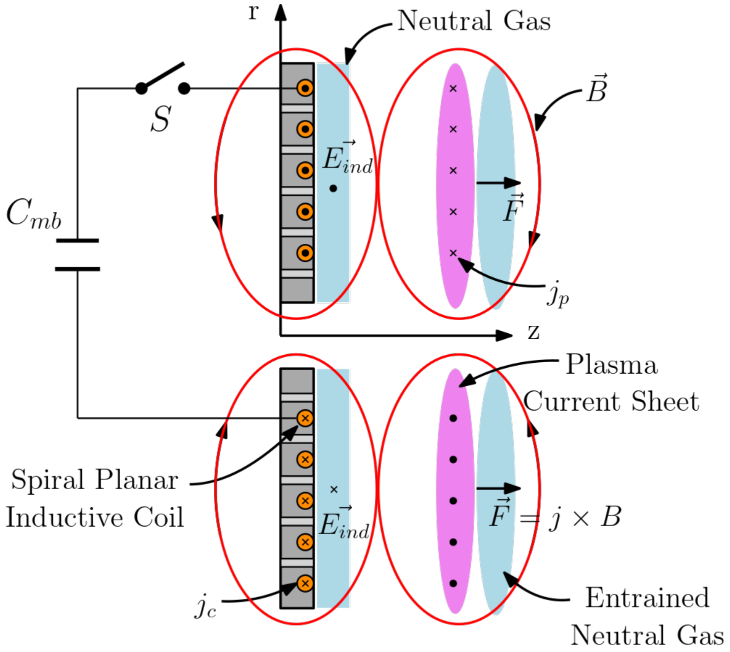

Figure 1.1: Schematic of basic IPPT operation. A neutral gas is injected and ionized from an azimuthal electric field in the direction of the coil current density j_c. The ionized gas then forms a plasma current sheet of current density j_p accelerating due to the Lorentz force $F = j_p \times B_r$, bringing any entrained gas with it.

and sheet thus accelerating the sheet away and any entrained particles producing thrust. This type of electrical propulsion device has the advantage of having no electrodes in direct contact with the plasma, thus increasing its potential lifetime compared to other electric propulsion devices such as traditional PPT's, ion, or hall thrusters. This advantage also allows IPPTs to use more corrosive propellants such as hydrazine which would typically damage the thruster. This thesis focuses on a variant of IPPT called the High-Pulse-Rate Pulsed Inductive Thruster (HiPeR-PIT). HiPeR-PIT, as its name suggests is an IPPT with a goal of operation on the order of hundreds of thousands of energy pulses a second.

1.1 HiPeR-PIT Concept

In order to understand the IPPT model, it is important to understand the basic physics behind operation of an IPPT. To operate an IPPT, a capacitor bank with capacitance C_o is charged to an initial voltage, typically on the order of kilovolts. Neutral gas is then injected through the coil face, and a switch is activated to discharge the energy through the coil resulting in high varying currents. With sufficient energy, the gas near the coil face ionizes and the Lorentz force produced between the plasma and coil produces thrust.

First a capacitor bank with capacitance C_o is charged to an initial voltage on the order of 1-100 kV. Holding this amount of voltage requires switches which are capable of handling high voltages as well as high currents on the order of 10s of kA [22]. The voltage and energy stored depends on the requirements of the device and is dependent on coil size. Smaller devices such as the HiPeR-PIT cannot reach higher voltages safely, however, this is accounted for by an initial energy pulse to pre-ionize the gas before the full energy pulse. Other small devices such as the FARAD [26], described by Polzin, use pre-ionized gas from other sources such as a helicon source.

Gas injection is crucial in an IPPTs operation with an ideal gas distribution that is uniform in density along the coil face. There are multiple methods of gas injection such as the magnetic field assisted injection seen in FARAD, or the backward nozzle seen in the PIT MK V [5], but in the case of the HiPeR-PIT, gas is injected through holes in the coil face. After gas injection, a high voltage, high current capable switch is then closed which sends a large varying current through the coil face. The current induces magnetic fields according to Ampere's law,

$$\nabla \times \boldsymbol{B} = \mu_o \boldsymbol{J} \tag{1.1}$$

Here current, J, is in the azimuthal direction, $\boldsymbol{J} = j_\theta \hat{\theta}$ and the magnetic field is radial, $\boldsymbol{B} = B_r \hat{r}$. Since the current varies temporally, the magnetic field is also changing resulting in an electric field through Faraday's law,

$$\nabla \times \boldsymbol{E} = -\frac{\partial \boldsymbol{B}}{\partial t} \tag{1.2}$$

Where the electric field, E, is in the azimuthal direction, $\boldsymbol{E} = E_\theta \hat{\theta}$. As stated above, the azimuthal electric field can ionize the gas if the energy of the system is high enough. Larger

IPPT devices such as the PIT MK V have enough energy flow through the coil to ionize the gas in the early stage of the current pulse, but in the case of the markedly smaller HiPeR-PIT, a smaller pulse is first used to help pre-ionize the gas. Coil design is also an important factor for IPPT operation, and their are multiple design from a traditional Archimedes style, to coils with a conical angle. For the purposes of this thesis, coil design will focus on the two turn Archimedes spiral presented by Polzin et al. [22] . Once the propellant is sufficiently ionized, the ionized particles begin to interact with the induced magnetic field produced from the coil current by forming a counter current and a counter magnetic field. This rotating mass is known as a plasma current sheet, and as the sheet gains ionized particle density, it becomes impermeable to the magnetic fields from the coil. The magnetic pressure $B^2/(2\mu_0)$ between the current sheet and coil and the resultant Lorentz force causes the sheet and coil to repel each other accelerating the plasma current sheet downstream of the coil, thus generating thrust.

1.2 Current Sheet Formation

Current sheet formation is crucial for the basic function of an IPPT and is one of the main focuses of this thesis. The strength of current sheet formation dictates the permeability of the accelerating mass to both the electromagnetic fields of the acceleration coil and the neutral particles the sheet comes into contact with. A strong current sheet can be defined by the following characteristics:

- A high ionized particle density n_s such that the current sheet is impermeable to the magnetic fields from the coil. As described by Jahn [10], the external coil circuit is complete in an IPPT without plasma unlike that of a traditional PPT. This means that any energy pulsed will be lost as the magnetic fields from the coil permeate through to infinity should a plasma sheet not be formed for said energy to be deposited into.

- Dense enough such that the sheet is impermeable to neutrals ensuring that any neutral particle interacting with the sheet either ionizes or is entrained in the current sheet, thus contributing to the overall thrust and mass efficiency. Neutrals that remain or leave the chamber slower than the current sheet result in reduced mass efficiency.

- Near instantaneous formation near the coil face. Current sheet formation must occur on sub microsecond timescales in order to entrain the highest amounts of neutral gas. Current sheets which form too slowly may be accelerated by the coil before full formation, leaving behind propellant and losing energy due to the decreased mutual inductance from an increased distance from the coil. It is also desirable to have most entrainment occur at the coil face as collisional and ionization losses further from the coil energy pulse result in greater energy losses.

A weak current sheet will thus suffer from permeability to neutral gases and electromagnetic fields leading to thruster inefficiencies.

While current sheet formation is the basis for operation of an IPPT, attempting to get a strong current sheet requires several conditions. Polzin [26] specifies a necessity for some value of ionized particle number density n_s for a coil with a specified current rate dJ/dt. While experiments such as the PIT have energy on the order of kJ, which can ionize and accelerate propellant from a neutral state, low energy experiments such as the FARAD and HiPeR-PIT require pre-ionzation to reach this critical n_s value. Currently it is assumed that the energy required for current sheet formation is negligible compared to the energy which is deposited into acceleration of the current sheet itself, however this may not be the case for vast array of propellants available to an IPPT which may also lead to efficiency losses.

1.3 Previous Work

IPPT experiments have been occurring since the 1960s, a period in which the greatest strides were taken to advance the technology. However, since that time, there have been several other experiments of note that have sought to both decrease the energy requirements of IPPTs and innovate on the design such as coil geometry. The following are some of the highest profile IPPT experiments of note.

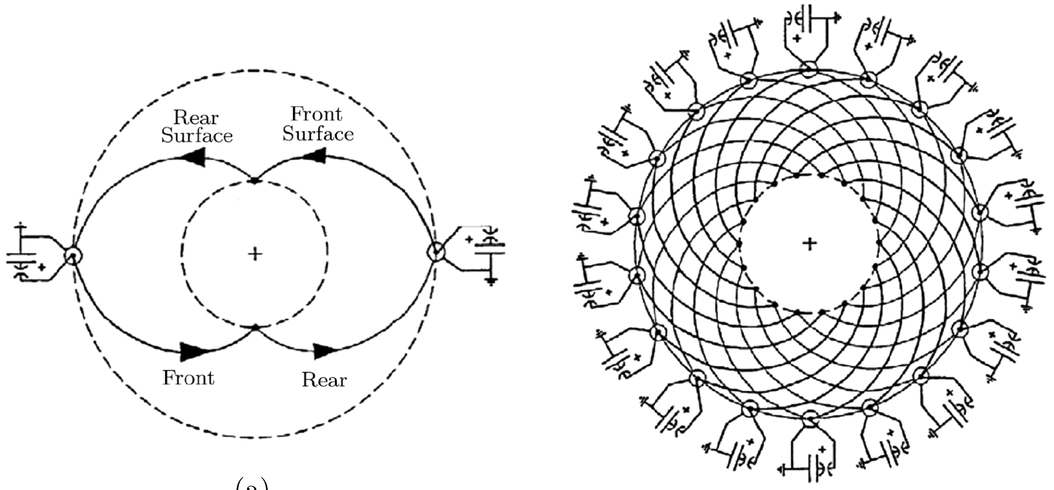

(a)

(b)

Figure 1.2: Schematics of a single complete Marx loop a), and a complete Marx coil configuration b) (from [5]).

1.3.1 PIT MK V

The Pulsed Inductive Thruster (PIT) is a planar type IPPT coil researched by Lovberg and Dailey [5] from 1960s-1990s. The PIT is currently still the state-of-the-art for pulsed inductive acceleration and has the highest amount of literature and research. The PIT has been iterated several times with the most significant iterations being the PIT MK V and MK Va, which saw the implementation of the Marx-bank configuration, shown in Fig. 1.2, from the original Archimedes spiral coil and single capacitor bank of previous PIT designs. The Marx-bank allows for a doubling of the applied coil voltage compared to the voltage of the individual capacitors, which turns the original capacitor charge from ∼15 kV to ∼30 kV of effective voltage. Stray inductance of the coil circuit was also kept at a minimum due to the parallel configuration of the Marx-bank. A higher initial voltage and low stray inductance allowed for a higher current rise rate than the previous iterations of the PIT, which directly improved the initial ionization time of neutral gas.

A schematic of the PIT MK V can be seen in Fig. 1.3. The PIT used a pulsed backwards

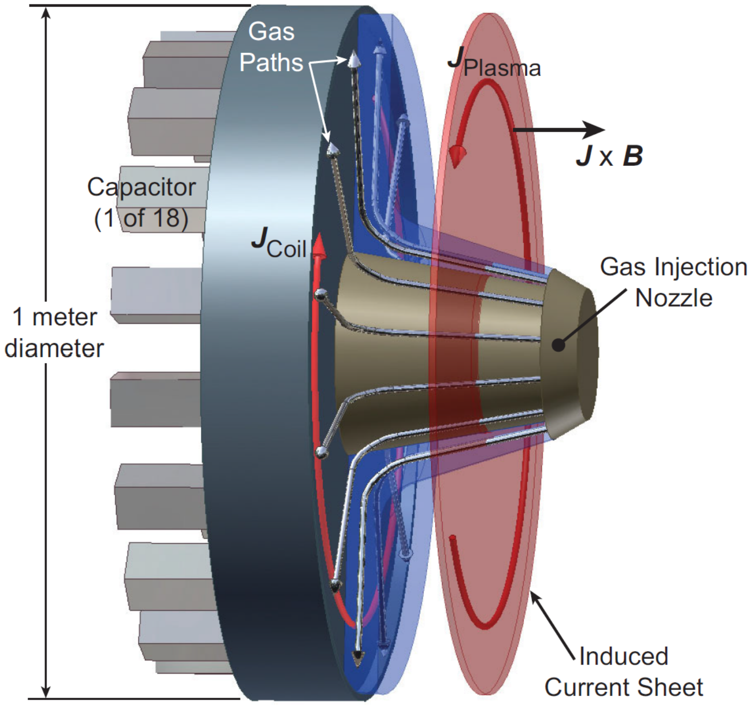

Figure 1.3: Schematic of the PIT MK V and its key features such as the backward facing nozzle, capacitor bank layout, and basic operation (from [26]).

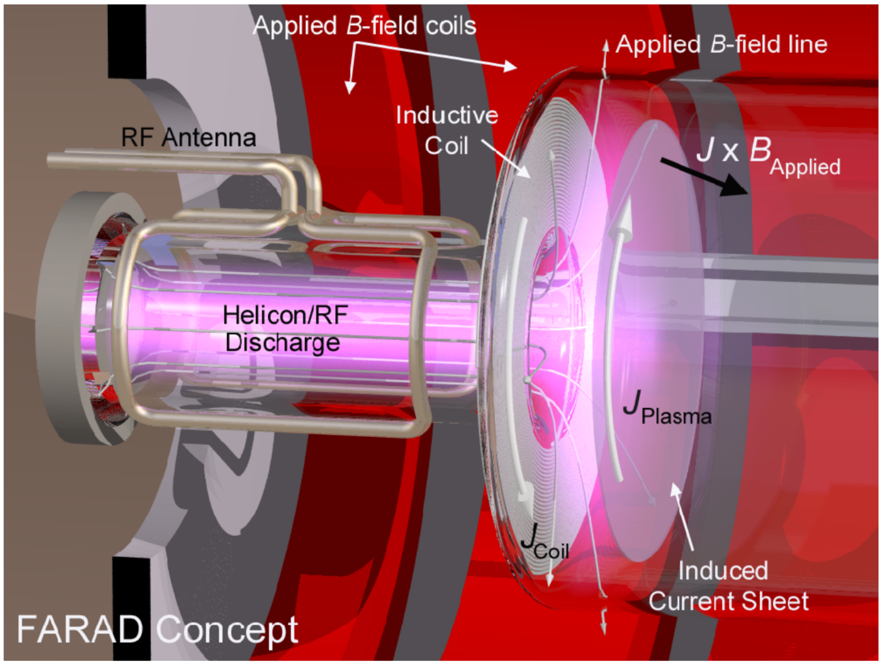

Figure 1.4: Concept art of the FARAD which shows the pre-ionization Helicon/RF stage as well as distribution of the pre-ionized gas across the coil face from the applied magnetic fields (from [26]).

facing nozzle placed within the center of the coil to deliver gas evenly across the coil face as depicted in Fig. 1.3. Gas was injected through the nozzle which redirected the gas back towards the coil and radially over the coil face with a near uniform distribution [5, 16]. The PIT MK V had a coil diameter of 1 m with 18 coil half turns. Coil size is related to the coupling distance, the region over which the coil interacts with the plasma current sheet. By having a larger coil, this distance could be increased, allowing for further coupling for energy deposition. The shear scale of the PIT with a 1 meter wide coil and large energy requirements has sparked a plethora of IPPT experiments seeking to decrease the energy per pulse requirements.

1.3.2 FARAD

Another PIT experiment of note was the FARAD or Faraday Accelerator with RF Assisted Discharge as described in detail by Polzin [26] and Choueiri [2]. The FARAD device was a experiment which explored the use of pre-ionization in a low energy PIT device. FARAD consisted of 12 half-turn coils and a coil outer diameter of 20 cm connected to a 39.2 μF capacitor bank. The FARAD had a discharge energy of ∼44-78.5 J/pulse. At these lower energies, it is difficult to breakdown the coil gas during the initial energy pulse of the acceleration coil, especially within the time frame necessary to prevent the gas from accelerating away. Using pre-ionization, the FARAD in theory would be able to form a current sheet close to the coil face for the highest possible energy deposition. The FARAD concept art is shown in Fig. 1.4. Pre-ionization was accomplished via a helicon/RF antenna to ionize gas in a chamber behind the coil. Applied magnetic fields were then used to guide the now ionized particles from the ionization chamber across the coil face. This pre-ionization method was not without its issues, as the applied magnetic fields could not be made tight enough to create a densely populated uniform region of pre-ionized particles over the coil face as was desired. This led to inefficiencies in the FARAD during current sheet formation and led to overall weaker current sheets.

1.4 Thesis Scope and Outline

This thesis seeks to explore the physics underway within the HiPeR-PIT to aid in the design and development of the thruster through both physical experimentation and numerical analysis of the HiPeR-PIT current sheets. By determining current sheet formation at several capacitor configurations, energies, and gas pressures, optimal conditions can be identified for operation of the HiPeR-PIT. The outline of this thesis is as follows: In the following chapter, a one dimensional model is formulated and the single pulse numerical study is analyzed. Chapter 2 covers the experimental setup of the HiPeR-PIT. In chapter 3, several diagnostics used for plasma sheet identification are presented. Chapter 4 presents and analyzes the experimental data from the HiPeR-PIT experiment diagnostics, ending with a summary of these results. Finally we conclude with a summary and comparison of the experimental and numerical results with an analyses on potential improvements to design and reasoning behind deviations to the ideal numerical case.

Chapter 2

THE ONE-DIMENSIONAL MODEL OF IPPT THRUSTERS

The IPPT model can be simplified to two inductively coupled circuits. One circuit is a simple LCR circuit with capacitance equal to the circuit capacitor banks, circuit resistance and inductance of the IPPT coil. The aforementioned circuit is then coupled to the plasma circuit with resistance equal to the resistance of the plasma. The IPPT model used in this thesis is well described in a paper by J. Little, et al. [13], but it will be reiterated here for reference. The one dimensional model can be split up into two portions, the circuit model, and the plasma model.

2.1 Circuit Model

The circuit model is adapted from the circuit model by Martin and Eskridge [18] as well as Polzin and Choueiri [24]. The circuit is shown in Fig. 2.1. The IPPT is shown on the left side modeled as a capacitor with capacitance (C) connected in series with an acceleration coil with inductance (L_c) and circuit resistor of resistance (R_c). There is also a stray inductance modeled in series with the circuit as (L_o) and the circuit is controlled through a switch. On the right side, the plasma is represented as another floating circuit with inductance (L_c) and plasma resistance (R_p). These two circuits can be combined through the mutual inductance M between the acceleration coil and plasma.

Applying Kirchoff's law to the circuit model shown in Fig. 2.1 provides the following ordinary differential equations for coil the time evolution of the circuit current (I_c), plasma current (I_p), and voltage across the capacitor (V).

$$I_c' = \frac{(L_cV + (MI_c + L_cI_p)M' - R_pI_pM - R_cL_cI_c}{L_c(L_0 + L_c) - M^2} \tag{2.1}$$

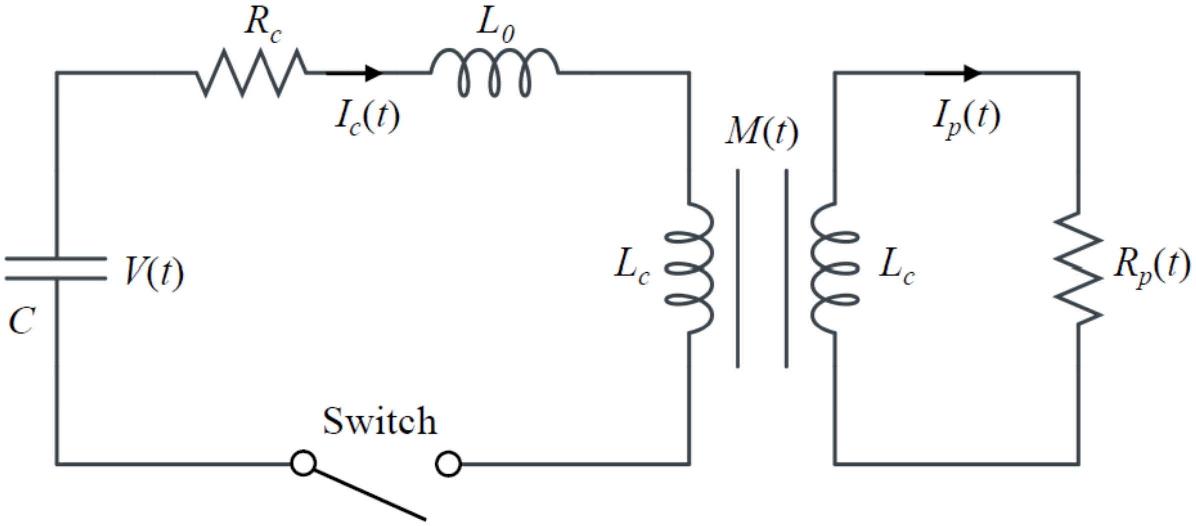

Figure 2.1: Lumped circuit model diagram of IPPTs showing the acceleration circuit on the left and plasma circuit model on the right (from [13]).

and

$$I_p' = \frac{MI_c' + I_cM' - R_pI_p}{L_c} \tag{2.2}$$

and

$$V' = -\frac{I_c}{C} \tag{2.3}$$

where the $'$ denotes a derivative w.r.t. time $y' = dy/dt$.

2.1.1 Mutual Inductance

Mutual inductance in the circuit is dependent on the distance between the acceleration coil and the plasma current sheet. This relationship has been shown to be exponential [15], and can be modeled as

$$M = (1 - \Theta_e)L_ce^{-(z_s - z_a)/z_c} \tag{2.4}$$

where z_s is the distance between the acceleration coil and plasma sheet, z_c is the decoupling length of the coil, and z_a is the distance from the coils to the acceleration coil face. Θ_e

represents the transparency of the plasma to the electromagnetic fields from the acceleration coil where $\Theta_e \in [0,1]$. Several plasma models have been produced for IPPTs before that assume the plasma current sheet is impermeable to accelerating fields from the start of its formation. This allows M to only be a function of the distance between the current sheet and acceleration coil. However, impermeability has been shown to not be guaranteed in a current sheet, thus this model includes a transparency factor which dictates permeability to the accelerating fields to the plasma. Θ_e or electromagnetic transparency corresponds two two limits, a perfectly conducting plasma where $\Theta_e \to 0$ or $\Theta_e \to 1$ a completely transparent plasma where all electromagnetic fields permeate through thus transferring zero energy. Electromagnetic transparency relies on the characteristics of the current sheet where we can assume that the plasma is a uniform conductor with a skin depth δ_s. This gives an equation for electromagnetic transparency as

$$\Theta_e = e^{-cw_s/\delta_S} \tag{2.5}$$

Where w_s is the sheet width and the constant c is held at a value of 3 to give about 5% transparency δ_s whenever w_s=δ_s which corresponds to values found in previous experiments performed by Dailey and Lovberg [6].

2.2 Plasma Model

In previous IPPT models, propellant mass was modeled through the slug model, in which all mass was contained within the initial current sheet, or the snow plow model in which all mass was entrained as the current sheet moves downstream [10]. These models are limited by the assumption of impermeable sheet formation, which prevents observations in sheet formation which is one of the focuses of this thesis. The current model addresses this issue by providing equations which observe the sheet mass entrainment throughout the plasma formation process up to equilibrium. The geometry of the plasma model can be seen in Fig. 2.2. The origin of the model is the plane of the acceleration coil face. From this plane several

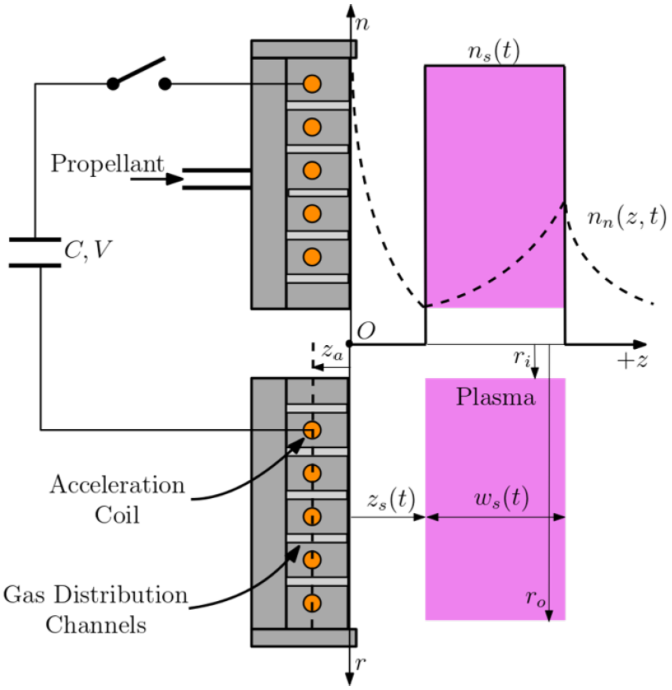

Figure 2.2: Visualization of several parameters calculated by the one-dimensional model (from [13]).

distances are measured such as distance to the coil z_a, and distance to the current sheet z_s. Time-evolving properties such as sheet width, sheet location, and sheet density can be seen with n_s denoting ionized particle density and n_n representing neutrals. The plasma inner r_i and outer r_o radius is also assumed to be equal to the radius of the coil.

2.2.1 Conservation of Mass

In addition to the circuit model, a volume-integrated multi-fluid model is used to model characteristics of the plasma current sheet. The propellant mass entrainment is modeled through the non-equilibrium continuity equation while incorporating electron impact ionization and charge-exchange collisions. Here it is assumed that three-body and dielectric recombination are negligible. Since convective transport of neutral particles occurs on timescales which are much slower than the period of the discharge circuit, the neutral continuity equation can be expressed as

$$n_n' = \begin{cases} 0 & z < z_s \\ -(S_{ion} + \sigma_{cx} v_s) n_n n_s & z_s \leq z \leq z_s + w_s \\ 0 & z > z_s + w_s \end{cases} \tag{2.6}$$

Here S_{ion} is the ionization reaction rate, n_n is the neutral particle number density, v_s is the sheet velocity, and σ_{cx} is the charge-exchange cross section. $n_n(z,t)$ is the only variable in this model that depends on both time and space. Having a spatial dependence allows the density to be tracked as the current sheet grows and accelerates from the acceleration coil. Since (2.6) is piece-wise, it can be assured that neutrals are only entrained in the current sheet when directly within the current sheet volume $z \in [z_s, z_s + w_s]$.

To conserve mass, the neutral gas particles which are consumed from ionization and charge exchange must appear elsewhere within the model. When undergoing ionizing collisions, neutral particles are transformed into ions, which requires a source term in the ion continuity equation to balance the ionization loss term from (2.6). Charge exchange collisions do not create new ions, but instead transfer momentum from a fast-moving ion to a slow moving neutral particle. This results in a neutral particle that moves at speeds much larger than the injected background neutrals. These "fast" neutrals are denoted as n_f and are modeled as a separate fluid from the plasma and "slow" background neutrals.

Integrating the plasma continuity equation (ion or electron) over the volume of the current sheet yields the following

$$(w_s n_s)' = n_s w_s S_{ion}(\bar{n}_n + n_f) \tag{2.7}$$

where

$$\bar{n}_n = \frac{1}{w_s}\int_{z_s}^{z_s+w_s} n_n dz \tag{2.8}$$

is the average density of the slow neutrals within the current sheet. (2.7) contains terms from two sources on the right-hand side. The first term represents ion-electron pairs through ionization of slow background neutral particles. The second term represents ionization of fast neutral particles leading to the creation of ion-electron pairs.

Accounting for the fast neutral portion of the fluid model and performing a volume integration of the continuity equation yields

$$(w_s n_f)' = n_s w_s(\sigma_{cx} v_s \bar{n}_n - S_{ion} n_f) - n_f \Delta v_{sf} H(\Delta v_{sf}) \tag{2.9}$$

Here the velocity difference $\Delta v_{sf} = v_s - v_f$ is the difference between the current sheet and fast neutral fluid velocities. A Heaviside step function is denoted by the H. The first term of the right-hand side describes the creation of fast neutrals through charge-exchange collision between the current sheet ions and background neutrals. The second term represents the loss of fast neutrals via electron-impact ionization in a Fokker-Planck model. The third term represents convective loss of fast neutrals from the trailing boundary or wake of the current sheet, a de-entrainment process referred to as "neutral slip".

Through Eq.(2.6), a new dimensionless parameter can be derived to describe the transparency of a current sheet to upstream propellant mass. Neutral particles are consumed by the current sheet with a frequency of $(S_{ion} + \sigma_{cx} v_s)n_s$. The amount of time the current sheet resides in the vicinity of said neutral particle is taken as w_s/v_s. Thus, the probability that a neutral particle is consumed by the current sheet can be shown as $\Theta_m = \Theta_{m,ion}\Theta_{m,cx}$, where

$$\Theta_{m,ion} = e^{-n_s w_s S_{ion}/v_s} \tag{2.10}$$

and

$$\Theta_{m,cx} = e^{-n_s w_s \sigma_{cx}} \tag{2.11}$$

where $\Theta_{m,ion}$ is the probability that a background particle will undergo ionization and $\Theta_{m,cx}$ is the probability said particle will undergo charge exchange while within the current sheet. Here we can see where previous IPPT models fit in with the snowplow model for mass entrainment becoming valid when $\Theta_m \to 0$. The current sheet becomes transparent in the limit of $\Theta_m \to 1$ allowing the neutral propellant mass to slip through without any reactions. This limit is known as the slug model in which all entrained propellant occurs at current sheet formation only.

2.2.2 Conservation of Momentum

Volume integration over the current sheet of the plasma fluid momentum conservation equations provides an expression for the acceleration of the current sheet and associated evolving mass

$$(w_s n_s v_s)' = (1 - \Theta_e)\frac{L_c I_c I_p}{m_i A_s z_c} e^{-(z-z_a)/z_c} - f_c \tag{2.12}$$

here the first and second terms of the right-hand side describe the Lorentz and collisional forces on the current sheet per unit area per unit atomic mass respectively. Eq. (2.6) introduces atomic mass of the propellant, m_i as well as the acceleration coil cross-sectional area, $A_s = \pi(r_o^2 - r_i^2)$. The Lorentz Force term described by Martin and Eskridge [18] has been modified to include transparency of the current sheet ($\Theta_e \neq 0$). Force due to background neutral pressure has been ignored as it was found to be negligible for the regime of interest.

Collisional force tracks momentum transferred from the current sheet due to charge-exchange and ionizing collisions and can be written as

$$f_c = (\bar{n}_n \sigma_{cx} v_s^2 + n_f \sigma_{cx} |\Delta v_{sf}| \Delta v_{sf} - n_f S_{ion} v_f) n_s w_s \tag{2.13}$$

The above equation represents momentum loss in ions due to charge exchange collisions and momentum gain in ions through ionization of fast neutral particles. Here we assume, 1) slow neutral particles are at a velocity much lower than the current sheet and thus do not contribute to momentum via ionization; 2) collisions between ions and neutrals are dominated by charge-exchange; and 3) the momentum transfer cross-section for electron-neutral collisions are negligible compared to those ion-neutral collisions.

Taking the volume-integral of the momentum equation for fast neutral particles yields

$$(w_s n_f v_f)' = f_c - n_f v_f \Delta v_{sf} H(\Delta v_{sf}) \tag{2.14}$$

here the charge-exchange collisions provide a source of momentum while ionization causes momentum loss. Momentum is also lost from slippage of entrained neutrals at the trailing boundary of the current sheet if $\Delta v_{sf} > 0$. Momentum Eq. (2.14) ignores force due to pressure gradients of the fast neutrals, an assumption which is valid when $(\lambda_f / w_s)(c_{s,f}/v_s)^2 \ll 1$. Here $c_{s,f} = \sqrt{k_b t_f / m_i}$ represents the fast neutral sound speed and $\lambda_f = (n_s \sigma_{cx})^{-1}$ is the mean-free-path for charge exchange. The only source of fast neutral thermal energy is the ion kinetic energy, limiting $(c_{s,f}/v_s) \lesssim 1$. Therefore, cases in which fast neutrals are abundant cause $(\lambda_f / w_s) \ll 1$, making the pressure force on fast neutrals small compared to the collisional force.

The kinematic equation also allows for the location of the current sheet to be resolved as

$$z_s' = v_s \tag{2.15}$$

here z_s represents the distance from the injection plane to the current sheet as shown in Fig.

2.2.

2.2.3 Conservation of Energy

The equations that have been presented so far form a closed system while assuming fixed values for plasma resistance R_p, skin depth δ_s, and ionization reaction rate S_{ion}. However these values depend heavily on microscopic processes within the plasma sheet which are strongly influenced by the electron temperature. It has been shown that energetics of inductive acceleration and propellant mass entrainment by the current sheet are dependent on the heating and cooling of the electron population within the plasma. For example, electron-impact excitation and ionization of neutrals decrease with electron temperature T_e while currents induced within the current sheet increase electron temperature through Ohmic heating. Timescales of the above processes vary with many aligning with that of IPPT plasmas thus they must be taken into account in terms of current sheet formation in the for of a non-equilibrium electron energy equation.

To get an equation for the time-evolution of T_e, the volume integral of the electron energy equation [8] for a uniform plasma. The electron kinetic energy and heat flux terms are neglected yielding the following

$$(n_s w_s T_e)' = \frac{2}{3A_s}(P_{ohm} - P_{en} - P_{ei}) \tag{2.16}$$

where

$$P_{ohm} = \frac{I_p^2 R_p}{e}, \tag{2.17}$$

$$P_{en} = S_{ion} n_s w_s A_s (\bar{n}_n + n_f)\varepsilon_{ion}^* \tag{2.18}$$

and

$$P_{ei} = \frac{3 m_e \nu_{ei}}{m_i}(T_e - T_i), \tag{2.19}$$

Here ε_{ion}^* is the effective ionization energy, ν_{ei} is the electron-ion Coulomb collision frequency, m_e is electron mass, T_i is the ion temperature, and e is the elementary charge. Eq. (2.16) gives the power gained by the current sheet from Ohmic heating P_{ohm}, the power lost to inelastic and elastic collisions P_{en}, and the power transferred through coulomb-coulomb collisions from electrons-ions interactions at a frequency of ν_{ei}.

P_{en} depends on the ion temperature, thus we need an ion energy equation to measure the temporal-evolution of T_i. The volume integral of the ion energy equation [8] with zero heat flux out of the sheet is described as

$$(n_s w_s T_i)' = \frac{2}{3A_s}(P_{ei} + S_{ion} n_s \bar{n}_n w_s A_s T_n) \tag{2.20}$$

This introduces T_n the background neutral temperature. The only terms in the ion equation are due to coulomb collisions and thermal energy from ionized neutrals. The terms associated with the rate of change of kinetic energy have been canceled due to Eq. (2.12). Ohmic heating also does not appear as plasma resistance R_p is dominated by the electron collision rate.

2.2.4 Current Sheet Width

The final time evolution needed to close the one dimensional model is the current sheet width. In previous IPPT models, current sheet width was assumed to be constant [17] or was evolved through diffusive processes within the plasma [15, 25]. This model seeks to understand how ionization processes affect the formation of current from the pre-ionized state, thus the rate of change of the current sheet width is given as

$$w_s' = \frac{D_p}{w_s} + (w_s')_f \tag{2.21}$$

here the first term represents the change in width resulting from the plasma diffusion, where diffusivity is D_p, and the second term $(w_s')_f$ shows the change in width due to the plasma formation process.

To model $(w_s')_f$, we must understand the internal structure of the current sheet as well as the associated electromagnetic fields. This information cannot be obtained from the circuit equations alone, thus approximations were made to estimate the value of $(w_s')_f$. The first assumption is the case when $w_s \geq \delta_s$, where it will be assumed that new plasma particles will accumulate in a distance $z \in [z_s, z_s + \delta_s]$. This is due the idea that the plasma current density which is azimuthal is strongest in the skin depth later which faces the acceleration coil, a region where local electron temperature and ionization rate is expected to be highest. This causes entrainment of neutral background gas to deposit newly ionized particles within said skin depth layer, which collapses the current sheet width w_s to skin depth δ_s at a rate which is proportional to that of the rate of new particles being entrained. For the case when $w_s < \delta_s$, newly created particles instead accumulate within $z \in [z_s, z_s + w_s]$, which suggests $(w_s')_f = 0$. A model for the above sheet behavior is shown below as

$$(w_s')_f = (\delta_s - w_s)H(w_s - \delta_s)\frac{N_s'}{N_s} \tag{2.22}$$

here the number of ions within the current sheet is calculated as $N_s = w_s A_s n_s$. The chain rule is used to expand N_s'/N_s which leads to the following equation used to find the rate of change of current sheet width

$$(w_s') = \frac{D_p}{w_s} + (\delta_s - w_s)(\frac{w_s'}{w_s} + \frac{n_s'}{n_s})H(w_s - \delta_s) \tag{2.23}$$

A closer look at the equation above reveals that $w_s \to \delta_s$ only when $D_p \to 0$ and that $w_s > \delta_s$ only if there is significant mass entrainment $[n_s'/n_s \gg 1]$. Should mass entrainment become exceedingly small $[n_s'/n_s \ll 1]$, the sheet width rate of change $w_s \to 0$ which is representative of the slug IPPT model.

2.2.5 Microscopic Processes

This one dimensional IPPT model has several parameters which depend on microscopic or particle scale processes that occur in the current sheet. These processes include r_p, δ_s, S_ion, σ_{cx}, ε_ion^*, ν_{ei}, and D_P and will be summarized within this section.

The first particle scale process is the plasma resistance, which is found through modeling the plasma as a conducting disk of uniform resistivity η_p, thus providing a resistance in the form of

$$R_p = \frac{\pi\eta_p}{min[w_s, \delta_s]}(\frac{r_o + r_i}{r_o - r_i}) \tag{2.24}$$

where the minimum expressed in the denominator is the width of the region where current flows within the current sheet. Plasma resistivity can be expressed as

$$\eta_p = \frac{m_e(\nu_{ei} + \nu_{en})}{n_s e^2} \tag{2.25}$$

here ν_{en} is the electron-neutral collision rate. The collision rate equations are modeled through the following electron temperature-dependent equations

$$\nu_{ei} = 2.91 * 10^{-12} n_s T_e^{-3/2} ln\Lambda \tag{2.26}$$

$$\nu_{en} = n_n \sigma_{en} \sqrt{\frac{8eT_e}{\pi m_e}} \tag{2.27}$$

here σ_{en} is the electron-neutral collision cross section and $ln(\Lambda)$ is the coulomb logarithm

$$ln(\Lambda) = \begin{cases} 23 - ln(T_e^{-3/2}\sqrt{n_s}) & T_e < 7.389eV \\ 24 - ln(T_e^{-1}\sqrt{n_s}) & T_e \geq 7.389eV \end{cases} \tag{2.28}$$

The diffusion coefficient D_p which controls the time-evolution of the sheet width can be found as

$$D_p = \frac{eT_e}{m_i(\nu_{ei} + \nu_{en})} \tag{2.29}$$

here the diffusion is ambipolar which coincides with the quasi-neutrality of the plasma current sheet. The last microscopic processes of note, sheet skin depth is expressed as

$$\delta_s = \sqrt{\frac{2\eta_p}{\mu_0 \omega}} \tag{2.30}$$

where the angular frequency of the electromagnetic field is $\omega = \sqrt{L_{eff}C}$, the effective inductance of the circuit is $L_{eff} = L_0 + (1 + k^2)L_c$, and the coupling efficient which changes with time is expressed as $k = M/L_c$.

Effective ionization energy is adopted from a model of plasma discharges produced by Lieberman and Lichtenberg [11], and is used to account for the electron energy lost through ionization, elastic polarization scattering, and line radiation. We model effective ionization energy as

$$\varepsilon_{ion}^{*} = \varepsilon_{ion} + \frac{1}{S_{ion}}(\sum_{j}(S_{ex,j}\varepsilon_{ex,j}) + \frac{3m_eT_eS_{es}}{m_iS_{ion}}) \tag{2.31}$$

where ε_{ion} represents the first ionization energy of the propellant being used, $S_{ex,j}$ and $S_{es,j}$ are the electron-impact excitation reaction rate and polarization scattering reaction rate respectively. $\varepsilon_{ex,j}$ is the energy for the j^{th} line transition. Finally, collision rates that involve electrons such as $S_{ion}, S_{ex,j}, S_{es}, \nu_{ei}$ and ν_{en} are modeled through a maxwellian electron energy distribution. This assumption is reasonable as the electron thermal time scales are expected to be ‘ faster within the current sheet when compared to that of the ions. The ion collision rates assume a cold ion population where $V_s \gg \sqrt{eT_i/m_i}$.

2.3 Argon Propellant Model

The one dimensional IPPT fluid model allows for analysis of both Xenon and Argon propellants, but the focus of this thesis will be on the use of Argon. The model estimates the mass of the propellant ions as $m_i = 1.67 * 10^{-27}W_a$ where $W_a = 39.95$ is the atomic weight of Argon.

The reaction rate coefficients for Argon in this model use a Maxwellian energy distribution which is fit to an analytical temperature dependent model. The following equations for the reaction rates are provided by Goldston, et al. [9]

$$S_{ion} = 2.34 \times 10^{-14}T_e^{0.59}exp(-17.44/T_e) \tag{2.32}$$

$$S_{es} = 2.336 \times 10^{-14} T_e^{1.609} exp(0.0618 ln(T_e)^2 - 0.1171 ln(T_e)^3) \tag{2.33}$$

$$S_{ex} = 2.48 \times 10^{-14} T_e^{0.33} exp(-12.78/T_e) \tag{2.34}$$

2.4 Model Initial Conditions and Inputs

The model forms a closed system of 13 Ordinary differential equations for the time-evolution of the state variables: $V, I_c, I_p, M, N_n, n_s, n_f, T_e, T_i, z_s, w_s, f_s, v_f$ through equations (2.1)-(4),(6-7), (9), (12), (14-16), (20), (23). These variables require initial conditions for the equations to resolve. The first initial conditions assume a stationary pre-ionized plasma $[v_s(0) = v_f(0) = 0]$ with an initial width $[w_s(0) = w_{s,0}]$ and location of $[z_s(0) = z_{s,0}]$. Pre-ionziation is modeled as $\chi_i(z) = n_{i,pi}(z)/n_{n,inj}(z)$, where $n_{n,inj}(z)$ is the injected neutral density profile before pre-ionization while $n_{i,pi}(z)$ is the ion density profile after pre-ionization. The initial profiles of the neutral density and plasma density respectively are described as

$$n_n(z, 0) = [1 - \chi_i(z)] n_{n,inj}(z) \tag{2.35}$$

and

$$n_s(0) = \int_{z_{s,0}}^{z_{s,0}+w_{s,0}} \chi_i(z) n_{n,inj}(z) dz \tag{2.36}$$

Initially, it is assumed that the plasma current sheet contains zero fast neutrals $[n_f(0) = 0]$. This assumption allows the initial density profiles to be derived using only two functions, $\chi_i(z)$ and $n_{n,0}(z)$. The model also requires initial electron and ion temperatures $T_e(0) = T_{e,0}$ and $T_i(0) = T_{i,0}$. This model requires some level of pre-ionization as it cannot model the initial ionization of propellant gas.

In regards to modeling the acceleration coil, the capacitor main bank is initially charged to a voltage of V_0 where time $t = 0$ is the moment where the switch closes the circuit therefore providing initial conditions $V(0) = V_0, I_c(0) = 0$, and $I_p(0) = 0$. Lastly, the mutual inductance $M(0)$ is found using the transcendental equation $k_0 = M(0)/L_c$ where

$$k_0 = e^{(-z_{z,0}-z_a)/z_c}[1 - e^{-3w_{s,0}/\delta_{s,0}(k_0)}] \tag{2.37}$$

here k_0 is derived from the initial plasma skin depths consistency with $M(0)$ through L_{eff} [25].

To summarize, the model requests inputs for the acceleration coil circuit (C, R_c, L_0, L_c), the coil geometry (r_i, r_o, z_a, z_c), the gas propellant $(m_i, S_{ion}, \varepsilon_{ion}, S_{ex,j}, \varepsilon_{ex,j}, S_{es}, \sigma_{cx})$, neutral gas distribution $(n_{n,0}, T_n)$, and the pre-ionized gas distribution $(\chi_i, w_{s,0}, z_{s,0}, T_{e,0}, T_{i,0})$. These initial inputs will be used to create models of a single discharge under several cases.

2.5 Propulsion Performance Metrics

An advantage of modeling the early formation characteristics of a plasma current sheet is the ability to resolve several dynamic properties which correspond heavily from those initial physics.Several performance metrics have been derived and applied to the IPPT model to understand the propulsive performance of the thruster.

The first performance metric of note is the impulse bit (I_{bit}) which is the total impulse provided from a single thruster pulse. The impulse bit is derived as

$$I_{bit} = m_i A_s[w_s(n_s v_s + n_f v_f) + \int_0^t n_f v_f \Delta v_{sf} H(\Delta v_{sf}) dt'] \tag{2.38}$$

The first term represents contributions from the ions, while the second and third terms represent contributions from the entrained fast and slipped fast neutrals respectively. $I_b it$ is evolves over the duration of the pulse with an asymptotic value which represents the total impulse provided from one energy pulse.

The specific impulse $I_s p$ is described as

$$I_{sp} = \frac{I_{bit}}{g_0 m_{bit}} \tag{2.39}$$

where m_{bit} is the mass bit, the total propellant added to the thruster prior to each pulse or

$$m_{bit} = m_i A_s \int_0^\infty n_{n,inj} dz \tag{2.40}$$

The thrust efficiency of the IPPT is derived as

$$\eta_T \equiv \frac{m_{bit}(g_0 I_{sp})^2}{2E_{tot}} = \frac{m_{bit}(g_0 I_{sp})^2}{2E_{pi} + C(V_0^2 - V^2)} \tag{2.41}$$

where E_{tot} represents the total energy of a single pulse, and E_{pi} is the energy of the preionized plasma $E_{pi} = n_{s,0} w_{s,0} A_s e[5/2(T_{e,0} + T_i, 0) + \varepsilon^*_{ion}(T_{e,0})]$. It is assumed that residual energy from a pulse is not lost but instead recaptured for use in later pulses [18].

Another propulsion metric, propellant mass utilization efficiency (η_m) represents the fraction of propellant that is accelerated to the velocity of the plasma where

$$\eta_m = \frac{g_0 I_{sp}}{v_s} \tag{2.42}$$

Mass utilization efficiency is modeled throughout each instant in the model to provide insight into how η_m evolves with time.

The final performance metric is the electrical efficiency η_e which describes the total kinetic energy of the accelerate propellant to the total input energy of the system. electrical efficiency is modeled as

$$\eta_e = \frac{m_i A_s [w_s(n_s v_s^2 + n_f v_f^2) + \int_0^t n_f v_f^2 \Delta v_{sf} H(\Delta v_{sf}) dt']}{2E_{pi} + C(V_0^2 - V^2)} \tag{2.43}$$

Here the first term of the numerator represents the kinetic energy of the ions, while the second and third terms represent the kinetic energy of the fast and slipped neutrals respectively. It should be noted that the thrust efficiency $\eta_T \approx \eta_m \eta_e$ when $n_s \gg n_f$.

Chapter 3

HIPER-PIT EXPERIMENTAL SETUP

This chapter describes all of the components of the HiPeR-PIT experimental setup. Each of the following components are assembled to create the HiPeR-PIT testing apparatus as shown in Fig. 3.1.

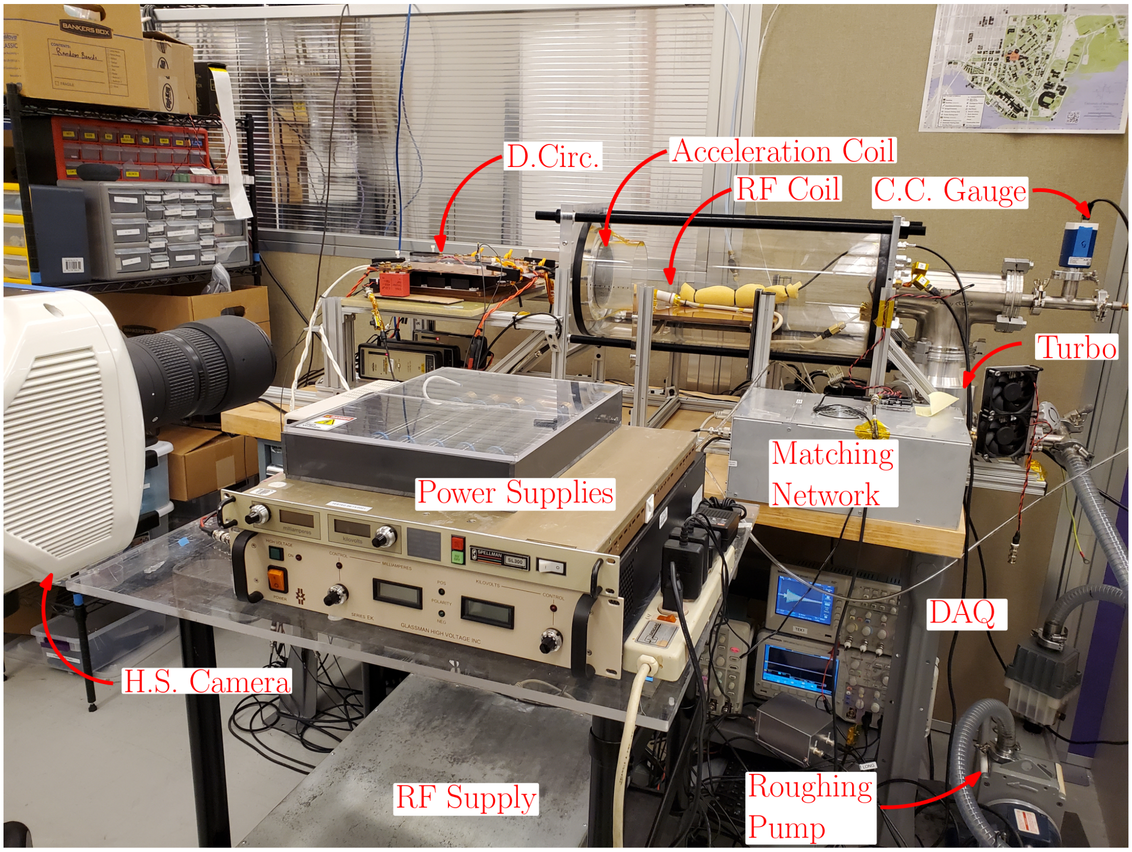

Figure 3.1: Experimental setup of the HiPeR-PIT experiment

3.1 Vacuum Chamber

The Vacuum chamber consists of a single cylindrical Pyrex glass tube about 25 cm (0.82ft) in diameter and 62 cm (2.03 ft) long with rubber L-gaskets on each end. These rubber gaskets form a gas tight seal in the glass chamber to plates on each side of the end points of the cylindrical tube. One plate is a 14x14x2 in. acrylic plate on which the inductive coil is mounted, while the other plate is 14x14x0.5 in. aluminum plate. The acrylic plate has a feedthrough for gas injection into a chamber which contains a porous Polymide foam that evenly distributes the gas before it enters through the coil backside and fills the region in front of the coil face. Two gas lines are attached to the chamber for regulation of gas mixtures through brass fittings. The aluminum plate has a 4 in. diameter hole in the center through which gas exits, 3 holes above sealed with hermetic BNC male adapters, and a hole on the side filled with two side-by-side Ethernet feedthroughs along with another BNC feedthrough. The chamber is attached to a Edwards RV12 roughing pump backing a 510 L/s turbo pump which allows the chamber to pump down to pressures of ∼6e-6 Torr with no gas injection. Chamber pressure is also maintained at several values during experiments ranging from ∼1-4.5e-3 Torr. The Edwards EXC120 turbo pump controller rests to the side of the chamber on a shelf out side of view. Chamber pressure was monitored using a KJL cold cathode/Pirani combination gauge and KJL-SPARC power supply and display, which also resides on a shelf to prevent RF noise, which outputs the chamber pressure with an accuracy of ±30%.

3.2 Discharge Circuit

The high voltages and currents needed to run the HiPeR-PIT required special care in development of the discharge circuit. A high-side IGBT (Insulated Gate Bipolar Transistor) switch design was implemented on a sliding platform on the gas injection side of the HiPeR-PIT apparatus as shown in figures 3.1 and 3.2. The discharge circuit consists of two 3300 V, 1200 A ABB 1200E330100 IGBT switches with custom gate driver boards for control. The

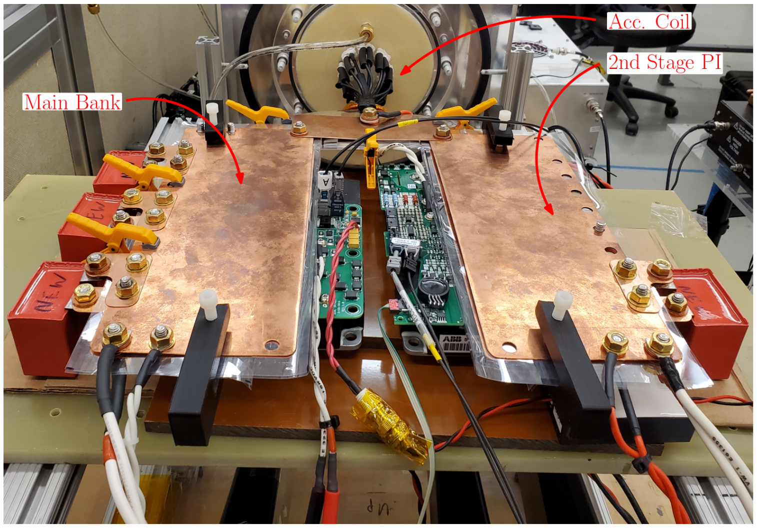

Figure 3.2: Photo of the discharge circuit for the HiPeR-PIT. The discharge circuit consists of a mainbank and 2nd stage pre-ionization bank connected to the inductive drive coil through high-side IGBT switches in parallel.

gate driver resistances have been dropped to increase the gate voltage allowing for higher current rates at large frequencies (∼100-300kHz). These switches were chosen to decrease energy losses due to the fast switching times present in the LCR acceleration coil circuit. The main bank switch is connected via a copper bus to high voltage capacitors with a total bank capacitance ranging from 1-3μF. The second switch is part of a second stage pre-ionization circuit which fires just before the main bank. On the pre-ionization side, a 0.33μF capacitor is connected with the pre-ionization switch. Capacitors are charged by two separate power supplies, a Glassman EK series power supply for the main bank, and a EZ GP-4303A for the pre-ionization side. The smaller EZ power supply feeds energy through a voltage step-up device to reach the required voltages of ∼1-2 kV. The switches are connected to a QC9520 pulse generator generator for triggering and are controlled by a python script along with all oscilloscope outputs. A 50,000 Ω high current resistor bank is used to dissipate the circuit energy from each pulse. There are five differential probes measuring voltage in the circuit at several places. One probe measures the voltage across the main bank side, while another

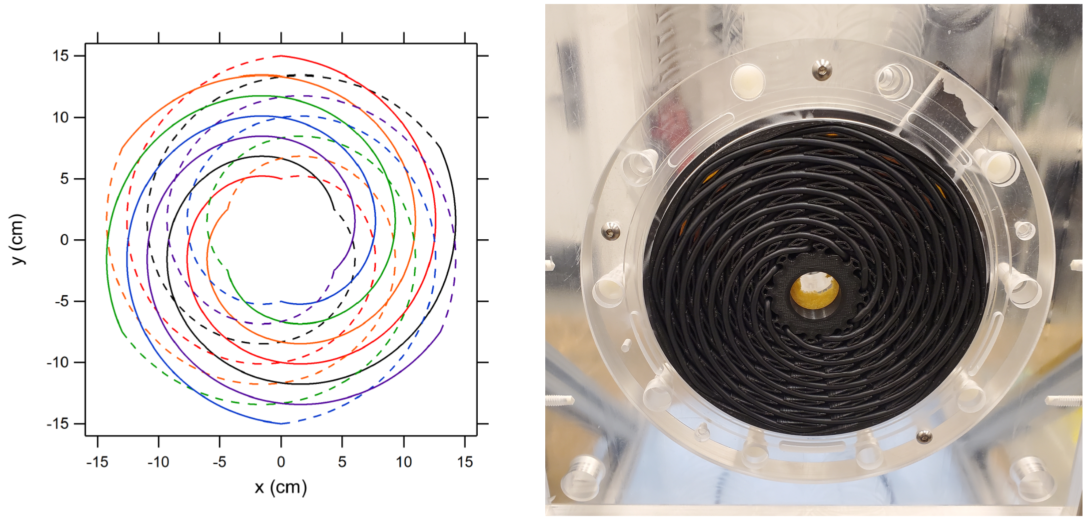

(a)

(b)

Figure 3.3: (a) Schematic of the two-turn Archimedes Spiral (from [22]). Each color represents another wire lead with the dotted leads running underneath the front leads. (b) Photo of the HiPeR-PIT coil. Here we can see the holes for gas injection as well as the Polymide foam for gas distribution

differential probe measures voltage across the pre-ionization side. A diff probe also measures voltage between the inductive coil connections. A Rogowski coil sits on the positive leads to the inductive coil to provide current measurements outside of the chamber. The first stage pre-ionization method uses RF pre-ionization in the form of an RF located within the chamber as can be seen in Fig. 3.1. The RF coil is powered by a Dressler CESAR RF Power Generator running at 100 Watt pulses.

3.3 IPPT Acceleration Coil

The acceleration coil for the HiPeR-PIT as shown in Fig. 3.3, is an experimental coil design described by Little, et al. [22], the two-turn Archimedes spiral. The two-turn Archimedes spiral allows for an addition of the azimuthal components of current flowing through the front and back leads, leading to a more uniform current density on the coil face. The HiPeR-PIT coil consists of 8 1.5-turn spirals, with 8 more 1.5-turn spirals returning underneath.

All the coil leads enter and return to the center region of the coil providing a ring of 16 wires through which energy is pulsed as shown in Fig. 3.2. The coil outer diameter is 6 in, while the inner diameter is 1.5 in. All coils are connected in parallel using battery bullet connectors sealed in vacuum-safe epoxy, which extend out the back of the acrylic bulkhead for ease of removal and installation. The center hole can either be plugged for vacuum or used in tandem with a pre-ionization device such as a RF coil. Polymide foam lays between the coil and the gas injection on the back of the acrylic bulkhead for even gas distribution within the coil chamber. Neutral gas is fed through the diamond shaped holes in the coils face, which are a resultant geometry of the Archimedes spiral. The coil itself resides within a 3d printed black PLA shell, which aids in image processing of the plasmas produced. The coil leads are made from 660/42 high-frequency Litz wire which has been insulated in heat shrink tubing for isolation form the plasma. Finally, A hollow transparent acrylic cylinder of radius 6 in. and length of 2.5 in. resides around the acceleration coil to keep gas and plasma in front of the coil face.

Chapter 4

PLASMA DIAGNOSTICS

Multiple diagnostics were used to examine current sheet properties in the HiPeR-PIT experiment. Other diagnostics were also incorporated to track characteristics of the acceleration circuit. The discharge circuit, oscilloscopes, and camera were triggered using a QC9520 pulse generator through a python script.

4.1 Rogowski Coil

Rogowski coils are a common current sensing device used in plasma diagnostics. A Rogowski coil consists of a loop of wire with another wire wrapped around forming a coil and central return loop as shown in Fig. 4.1. Any AC current flowing between the Rogowski coil induces a associated varying magnetic field which induces an electromotive force (emf). The current trace of the Rogowski can be derived from the induced voltage as

$$I(t) = \beta_r(\omega) \int_0^{\tau} V_{ind}(t)dt \tag{4.1}$$

where $V_{ind}(t)$ is the induced voltage, τ is total time of the signal, and β_r is the calibration or sensitivity factor which is obtained through calibrating the Rogowski against a known current source. In order to extract the current reading from Rogowski coils, the output must be integrated by either passing the signal through an integrator circuit or by numerical integration. The work presented in this thesis uses numerical integration applied to the Rogowski output voltage trace in order to prevent any potential phase shift caused by circuit integration. The Rogowski coil was calibrated against a 0.01 V/A high frequency current transformer. The Rogowski was placed on the positive lead of the acceleration coil along

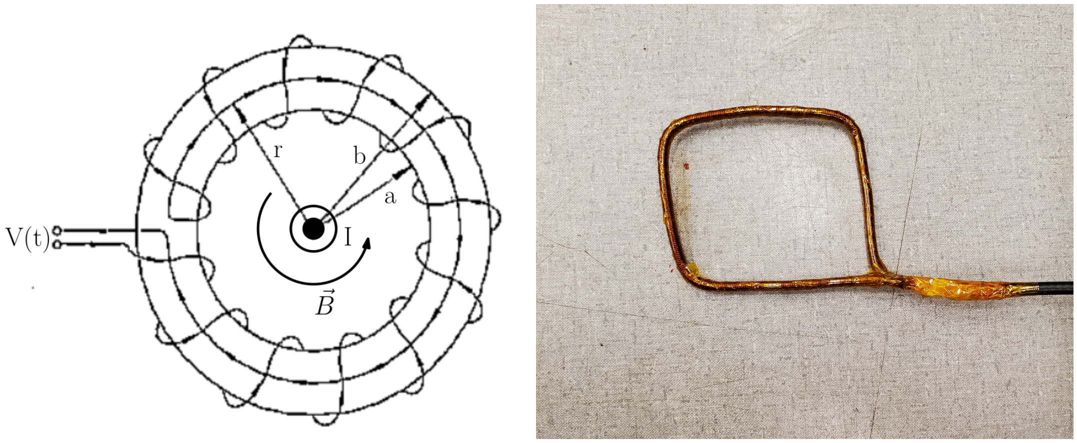

(a)

(b)

Figure 4.1: (a) Schematic of a Rogowski coil (after [28]). A coil of radius r, with outer and inner radii b and a respectively interacts with the magnetic field induced by an AC current flowing through the Rogowski. Since the magnetic field is varying due to a varying current, an emf is induced in the Rogowski coil loops. (b) Photo of the Rogowski coil used for current measurements.

with the current transformer, and several capacitance's ranging from 0.022-3 μF used in the main bank to vary the frequency of the current pulse from ~100-400 kHz. The sensitivity factor curve was determined using the following equation

$$\beta_r(\omega) = \frac{\int V_{ind}(t)dt}{I_c(t)} \tag{4.2}$$

where ω represents the frequency in Hz, and the numerator represents the integrated signal of the Rogowski and I_c is the current of the acceleration coil measured by the current transformer. Care needs to be taken when constructing Rogowski coils as several factors can affect the signal quality and response time. Inductance in a Rogowski coil is controlled by the number of coil turns around the return loop and the diameter of the turns. It is important to keep inductance low enough such that the Rogowski coil has a response time well below the current timescale being measured by the plasma. Output voltage of the Rogowski coil is also proportional to the inductance, therefore low inductance values may require amplifiers where as a high inductance could require signal attenuation before data acquisition. Capacitance is another key variable in construction of Rogowski coils, particularly stray capacitance. Capacitance in a Rogowski can be described by two types, capacitance between the coil turns which can be modeled as capacitors in series and is negligible, and capacitance between the coil turns and the return loop [28]. The stray capacitance between the coil turns and return loop can cause phase shift in the output waveform measured by the Rogowski compared to the actual currents produced. This phase-shift is not ideal when attempting to characterize multiple plasma sheet physics so caution must be taken to keep stray capacitance to a minimum. The most effective method of lowering capacitance was found to be insulation of the central return loop, however, adding insulation increased the diameter of the windings which in turn raised the inductance of the Rogowski coil, so care must also be taken to not add too much insulation. The completed Rogowski coil can be seen in Fig. 4.1b. Construction of the Rogowski coil consisted of a 18 AWG stranded wire loop which was pre-wrapped in insulation. 20 AWG magnet wire was then tightly wound around this central loop and one end was soldered together to attach the windings and the return. The un-soldered return loop end of the Rogowski was then soldered to the inner conductor of a coaxial cable, while the return loop of the Rogowski was soldered to the outer coax conducting shield. The soldered unshielded wires were then potted in 748 epoxy to prevent any gas breakdown near the leads. The entire array was then wrapped around with three layers of Kapton dielectric tape for insulation from any ionized particles and electrical fields. The dimensions of the Rogowski coil where a rectangle of height 6 cm and length 7 cm which allowed encirclement of exactly half of the acceleration coils annular discharge. The length allowed for resolution of the plasma current until complete dissipation. The Rogowski coil signal was fed through a PINTECH PT-8020 high voltage differential probe set to an attenuation of 1/100 so that it could be read safely through an oscilloscope. An estimate of the current density can be

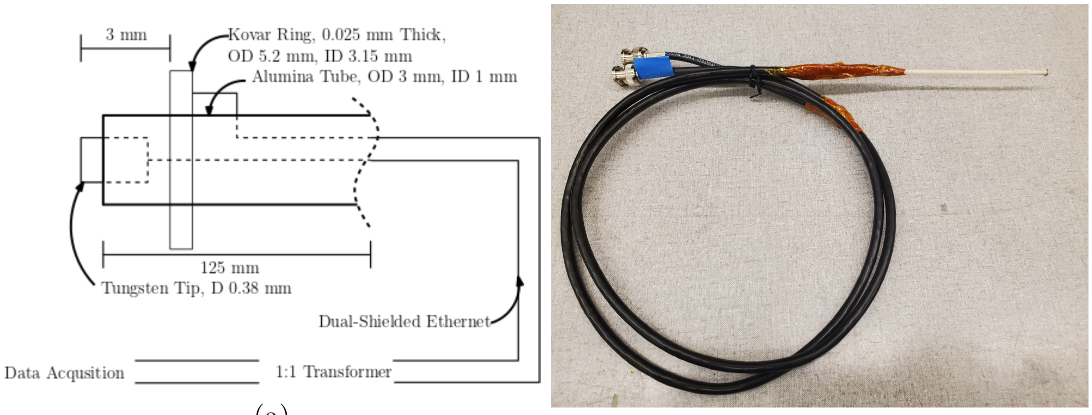

(a)

(b)

Figure 4.2: (a) Schematic of the electric field probe used for electric field measurements. (b) Photo of the electric field probe

found from the plasma current measured by the Rogowski coil as follows,

$$j_\theta = \frac{I_{p,\theta}}{w_s \times (r_o - r_i)} \tag{4.3}$$

where j_θ is the azimuthal current density, $I_{p,\theta}$ is the plasma current measured by the Rogowski coil, w_s is the plasma sheet width, and $(r_o - r_i)$ represents the height of the annular region of the acceleration coil which coincides with the height of the plasma.

4.2 Electric Field Probe

Floating electrodes are a common device used in plasma diagnostics to measure the electric fields. Floating electrodes as the name suggests, measure the floating potential of the plasma, kT_e/e, at two close points which allows for an estimate of the electric field as shown in the equation below

$$E = \frac{\Delta V}{d} \tag{4.4}$$

here ΔV is the difference in the potentials measured, and d is the distance between the two electrodes. The electric field probe used to acquire electric fields is based on the probe used and described by Lovberg [14]. Lovberg states that there are two main assumptions made in order for floating electrodes to accurately measure the axial electric field.

- First, in order to float at $-kT_e/e$, the electron flux to the probe tips must be significantly larger than that of the ion flux, which is a given as the potential measured by the electric field probe was much higher than the highest expected $-kT/e$ value. Here k is Boltzmann's constant, T_e is the electron temperature in eV, and e is the elementary charge.

- Second, the electron temperature must not have a significant gradient between the two probe tips [14].

These assumptions will be applied to the electric field probe. The electric field probe consists of two coaxial electrodes, a tip of tungsten 0.38 mm in diameter 3mm upstream from a ring electrode of diameter 5.2 mm and thickness 0.254 mm made of COVAR. The probe protrudes out of a 3.15 mm diameter tube of alumina as shown in Fig. 4.2 which houses the twisted pair wiring and connects to a coaxial cable with two BNC connectors, one for each tip. The connection to the BNC is shielded using silicone tape and kapton tape for isolation from the plasma, and the entire alumina probe assembly is sealed using Torr seal to isolate all components other than the electrode tips which are exposed to plasma. The E-Field probe connects to two perpendicular 1:1 transformers with 21 turns on the primary and secondary coils and an electrostatically shielded toroidal iron core which runs through the coils. This transformer allows for noise reduction with minimal attenuation of the source. The leads coming from the transformers are then passed through two Micsig DP10013 differential probes set at an attenuation of 50x to be read by an oscilloscope.

4.3 B-dot Probe

The time varying induced magnetic fields of the plasma and acceleration coil are measured using B-dot probes. The theory behind B-dot probes is discussed in detail by Polzin et

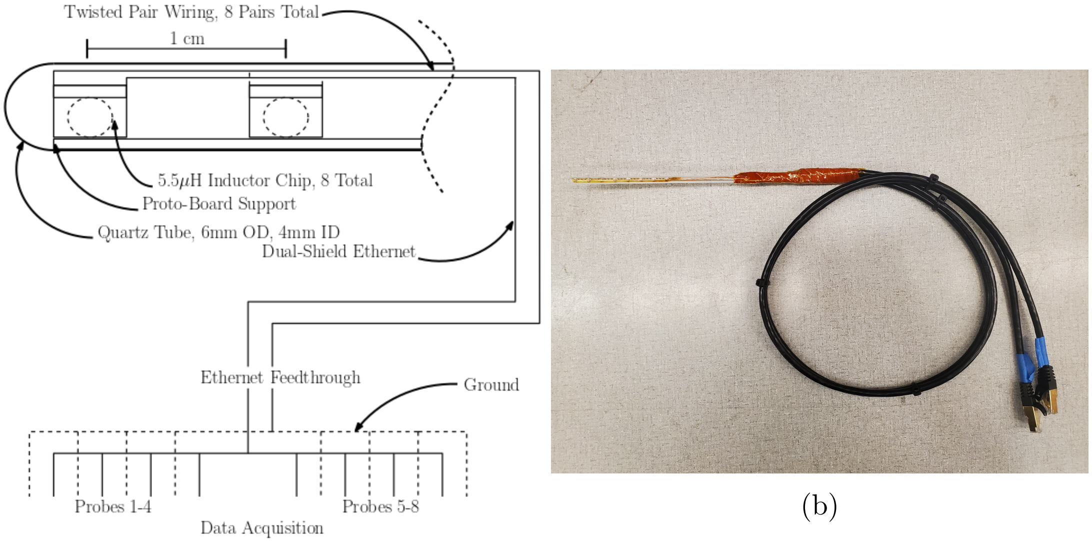

(a)

(b)

Figure 4.3: (a) Schematic of the B-dot probe used for magnetic field measurements. (b) Photo of the B-dot probe

al. [23]. A B-dot probe typically consists of a coil with N number of turns which resides in a region of time-varying magnetic fields. The magnetic fields induce an EMF in the coil as

$$\varepsilon = -NA_c \frac{dB}{dt} \tag{4.5}$$

Where A_c is the cross sectional area of the coil. The changing magnetic field can then be integrated over the time of the induced voltage signal to provide the magnetic field as

$$B = \beta_b(\omega) \int_0^\tau V_{ind}(t)dt \tag{4.6}$$

Here β_b, known again as the sensitivity factor of the probe, is a function of frequency and is obtained through calibration of the probe. A common method of calibration for B-dot probes, and the method used in this thesis, is the Helmholtz coil. A Helmholtz coil consists of two coils of equal radius, r_H, in series separated by a distance equal to the radius of one of the coils. This configuration produces a volume of uniform magnetic field in between the coils in the axial direction, which can be calculated as

$$B_H = (\frac{4}{5})^{3/2}\frac{\mu_0 N I_H}{r_H} \tag{4.7}$$

where I_H is the current flowing through the Helmholtz coil and N is the number of turns in the coil. The Helmholtz radius of the coils used for calibration was 3 cm. The sensitivity $\beta(\omega)$ of the probes can be determined using the known magnetic field of the Helmholtz coils as shown below

$$\beta_b(\omega) = \frac{\int V_{ind}(t)dt}{B_H(t)} \tag{4.8}$$

Here V_{ind} is the induced voltage across the B-dot probe. Several frequencies ranging from ∼100-500 kHz were used to form a sensitivity curve for calibration.

Construction of the B-dot can be seen in Fig. 4.3. The B-dot probe consists of eight 5.5 μH inductor chips with windings of size ∼1 mm spaced apart by 1 cm. The chips are epoxied on a support made of Proto-board which provides consistent orientation. The entire fixture resides within a 6 in. quartz tube of outer diameter 6mm and inner diameter 4mm. The inductor chips connect to 8 pairs of twisted wire leads which exit the tube to be directly soldered onto two dual shielded Ethernet cables. The connection between the tube and Ethernet is protected using silicone and Kapton tapes for isolation from plasma. The Ethernet cables are then fed to two Ethernet breakout boards which change the connection to BNC for direct connection to oscilloscopes. It was found that the signal produced by the B-dot probe was within the scopes range of voltage input for the experiments performed.

4.4 Plasma Density Estimates

An estimate of the plasma number density can be obtained using results from the plasma diagnostics listed thus far using a derivation described by Lovberg [6]. Starting with the generalized Ohm's Law,

$$\boldsymbol{E} + \boldsymbol{V} \times \boldsymbol{B} + \nabla P_e - \frac{\boldsymbol{j} \times \boldsymbol{B}}{e n_s} - \eta \boldsymbol{j} = 0 \tag{4.9}$$

Here we note the first major assumption of this plasma density estimate which is the setting of the resistivity η as a negligible value. This would typically hold true for a plasma in vacuum, however the high back-fill neutral densities of this experiment introduce a significant amount of resistance to the flow of the plasma through collisional forces which are ignored in this plasma density estimate. Moving on, we focus on the z component of the generalized Ohms Law which provides an equation for the azimuthal ion mass velocity as

$$V_\theta = \frac{E_z}{B_r} + \frac{j_\theta}{en_s} + \frac{T_e}{B_r n_s}\frac{\partial n_s}{\partial z} \tag{4.10}$$

where V_θ is the mass velocity or ion velocity. Setting the ion velocity to zero, representing zero ion current, and neglecting the electron pressure gradient term, we can derive a rough estimate for the plasma density as,

$$n_s = \frac{-j_\theta B_r}{eE_z} \tag{4.11}$$

where j_θ is the azimuthal plasma current density obtained through the Rogowski coil, B_r is the radial magnetic field obtained through the B-dot probes, e is the elementary electron charge, and E_z is the axial electric field from the electric field probe.

4.5 Differential Probes

Several PINTECH PT-8020 high voltage differential probes were used to determine the voltages of the acceleration circuit at multiple positions. Areas of interest were the 2nd stage pre-ionization capacitor bank voltage, the main stage capacitor bank voltage, and acceleration coil voltage. These differential probes were set to an attenuation factor of 1000. A Rogowski coil was also kept on the positive lead to the coil for measuring coil current through a Micsig DP10013 differential probe at a attenuation factor of 50. All traces were read through an oscilloscope.

4.6 Imaging

Imaging of the plasma current sheet was accomplished using two different devices, a High-speed camera, and DSLR. The coil material was made to be black to assist in image processing. Marks were placed on the side of the coil chamber starting from the coil face in centimeter increments to allow for estimates in current sheet position.

4.6.1 Kirana High-speed Camera

A Kirana high-speed camera was used identify current sheet formation and sheet position in the initial stages of the experiment. The Kirana is a 924x768 pixel camera capable of 7,000,000 FPS which allowed for high detail video of the current sheet from formation to dissipation. A fstop of 16 was used on the Kirana lens to prevent over saturation from high intensity plasma.

4.6.2 DSLR Camera

A DSLR was used to provide visualization of what the current sheet looked like with color. An fstop of 16 and an iso of 100 was used with a shutter speed set to 1/20. The DSLR was angled towards the coil face from the side of the vacuum chamber as a head on shot of the coil face was not possible in the current configuration.

Chapter 5

NUMERICAL AND EXPERIMENTAL OBSERVATIONS AND MEASUREMENTS

Data obtained through both experimentation on the HiPeR-PIT as well as the results of the one-dimensional model are resented in this chapter. A total of four cases were compared, a baseline case, a case where the backfill pressure was decreased, a case where the voltage of the main bank was increased (thus decreasing the pre-ionization), and a case where the capacitance of the main bank was doubled. The outline of this chapter will be as follows. First the one dimensional model results will be analyzed. Then observations of the visual data will be presented, followed by the plasma diagnostic measurements. Finally comparison will be drawn between the numerical model and experimental results and final thoughts on the current sheet formation will be presented.

The total energy for all cases ranged from ∼2-3.8 J/pulse depending on the capacitance and charge voltage which ranged from 1.5-2 kV per the limit on the switching capabilities. A backfill pressure ranging from ∼3.5 mTorr to ∼4.5 mTorr was used of Argon gas with the base case at 4.5 mTorr. At lower pressures, a current sheet does not seem to take shape, while the highest pressure presented is the limit of the current pumping capabilities of the vacuum chamber. Second stage pre-ionization used the same capacitor bank for all cases, a 0.33 μF high voltage capacitor. The RF 1st stage pre-ionization was operated at 100 W for all cases, while the second stage pre-ionzation was operated at a voltage of 1 kV for the high voltage case, and 1.5 kV for all other cases including the baseline.

Experimental conditions for the HiPeR-PIT experiment are summarized for each case in Table 5.1.

Table 5.1: Parameters between all cases.

Case	Voltage	Capacitance	Pressure	Energy
Base	1500 V	1.5 μF	4.5 mTorr	2.1 J/pulse
P↓	1500 V	1.5 μF	3.5 mTorr	2.1 J/pulse
V↑	2000 V	1.5 μF	4.5 mTorr	3.17 J/pulse
C↑	1500 V	3 μF	4.5 mTorr	3.75 J/pulse

The column designated as "Case" provides the notation for the different cases which will be used going forward. The shorthand represents changes in backfill or chamber pressure P, Main bank voltage V, or main bank capacitance C. Finally any experimental errors are reported with a 95% confidence bounds.

5.1 Numerical Model Results

Initial condition inputs for the numerical model are shown in Tables 5.2-5.2.

Table 5.2: Initial conditions for the baseline (Base) 1D study.

Variable	Value	Variable	Value	Variable	Value
V_0	1500 V	$T_{e,0}$	2.5 eV	$z_{s,0}$	0 mm
C_0	1.5 μF	$T_{i,0}$	0.1 eV	$w_{s,0}$	1 mm
R_c	5 mΩ	T_n	0.026 eV	$n_{n,0}$	1.44×10^{20} m^{-3}
L_0	50 nH	r_o	7.2 cm	$z_{a,0}$	-2 mm
L_c	0.43μH	r_i	2 cm	$z_{c,0}$	4 cm
χ_0	0.1	z_n	1 cm		

Table 5.3: Initial conditions for the decreased pressure (P↓) 1D study.

Variable	Value	Variable	Value	Variable	Value
V_0	1500 V	$T_{e,0}$	2.5 eV	$z_{s,0}$	0 mm
C_0	1.5 μF	$T_{i,0}$	0.1 eV	$w_{s,0}$	1 mm
R_c	5 mΩ	T_n	0.026 eV	$n_{n,0}$	1.12×10^{20} m^{-3}
L_0	50 nH	r_o	7.2 cm	$z_{a,0}$	-2 mm
L_c	0.43μH	r_i	2 cm	$z_{c,0}$	4 cm
χ_0	0.1	z_n	1 cm		

Table 5.4: Initial conditions for the increased voltage (V↑) 1D study.

Variable	Value	Variable	Value	Variable	Value
V_0	2000 V	$T_{e,0}$	2.5 eV	$z_{s,0}$	0 mm
C_0	1.5 μF	$T_{i,0}$	0.1 eV	$w_{s,0}$	1 mm
R_c	5 mΩ	T_n	0.026 eV	$n_{n,0}$	1.44×10^{20} m^{-3}
L_0	50 nH	r_o	7.2 cm	$z_{a,0}$	-2 mm
L_c	0.43μH	r_i	2 cm	$z_{c,0}$	4 cm
χ_0	0.1	z_n	1 cm		

Table 5.5: Initial conditions for the increased capacitance (C↑) 1D study.

Variable	Value	Variable	Value	Variable	Value
V_0	1500 V	$T_{e,0}$	2.5 eV	$z_{s,0}$	0 mm
C_0	3 μF	$T_{i,0}$	0.1 eV	$w_{s,0}$	1 mm
R_c	5 mΩ	T_n	0.026 eV	$n_{n,0}$	1.44×10^{20} m^{-3}
L_0	50 nH	r_o	7.2 cm	$z_{a,0}$	-2 mm
L_c	0.43μH	r_i	2 cm	$z_{c,0}$	4 cm
χ_0	0.1	z_n	1 cm		

Initial conditions stayed mostly the same between all cases with only changes in pressure, voltage, and capacitance inputs necessary. The initial neutral particle distribution $n_{n,0}$ was kept at a constant to simulate backfill conditions. The results of the numerical model study for each case are presented below.

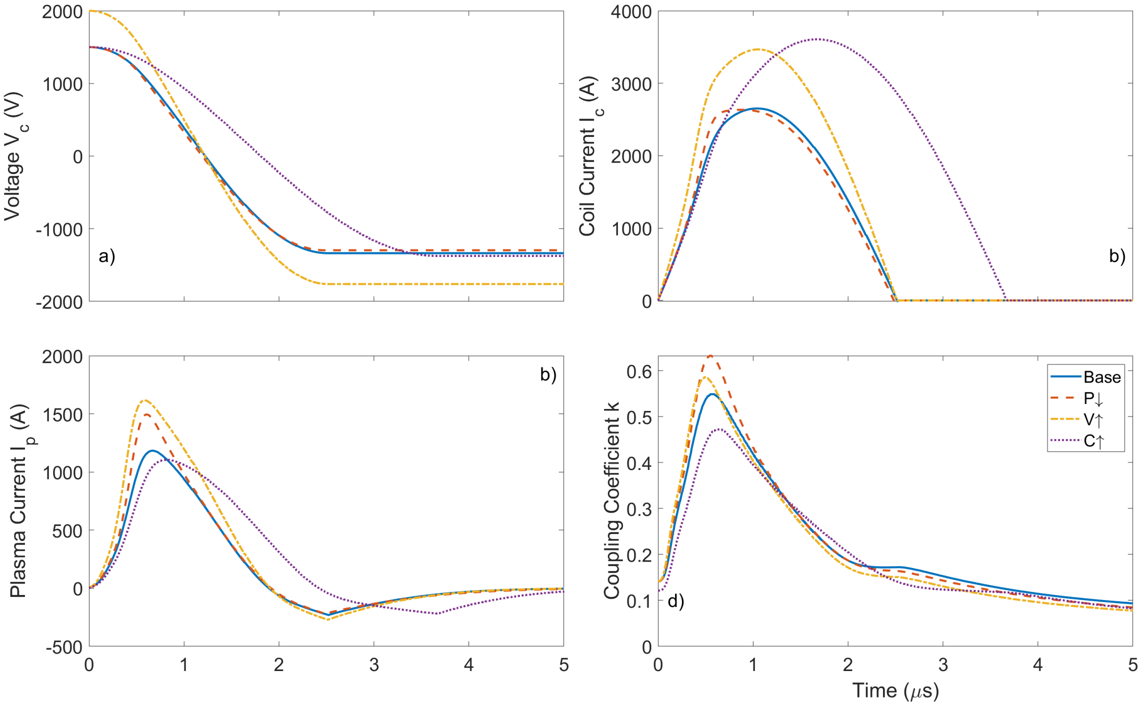

Figure 5.1: Plots of several derived plasma characteristics from the 1-D model for all four cases. Data is generated from the initial conditions presented in Tables 5.2-5.5.

We begin our analysis with results of several circuit parameters from the model, specifically the circuit voltage, coil current, plasma current, and coupling coefficient. The x-axis of each figure presents the simulation time in μs. Starting at Fig. 5.1a, the voltage traces decrease as expected from from 1.5-2 kV depending on the case. Discharge times vary according to the capacitance used, but in all cases the model switches off after one half cycle, to simulate inductive energy recapture, a process described by Polzin et al. [22]. Inductive recapture allows for reuse of the circuit energy for recharging after opening the switch mid ring down. Fig. 5.1b displays the current flowing through the coil for each case, which is 90 degrees out of phase with the voltage and not perfectly sinusoidal as there is a load applied to the inductive circuit due to the coupling of plasma. Fig. 5.1c presents the current flowing through the modeled plasma current sheet. We note here the decreased amplitude when compared to the coil current which is a behavior which should occur in experimentation as well. The plasma currents are skewed in nature due to the low coupling coefficients in early current sheet formation, seen in Fig. 5.1d. The case with the highest coupling coefficient was the case of lowest pressure followed by the case of increased voltage, baseline, and increased capacitance respectively.

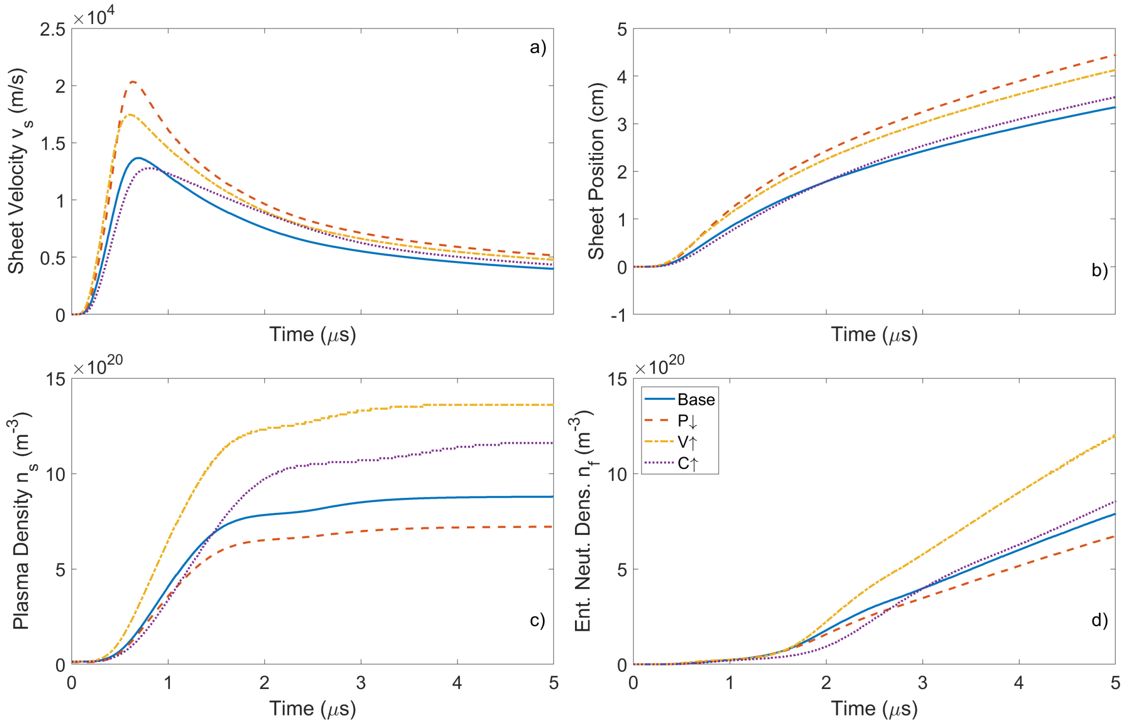

Figure 5.2: Plots of several derived plasma characteristics from the 1-D model for all four cases. Data is generated from the initial conditions presented in Tables 5.2-5.5.

Fig. 5.2 presents the sheet velocity and position as well as the plasma and entrained neutral densities. In Fig. 5.2a we see that the highest sheet velocity occurs in the case of the lower pressure which is due to the lower neutral background density providing less resistance to the motion of the current sheet. All cases accelerate until about $\sim$1 μs where frictional forces with the background neutrals overtake the Lorentz force provided by the acceleration coil thus decelerating the sheet. The same trend is seen in Fig. 5.2b which shows the low pressure sheet moving away at a higher velocity then all the other cases. The slowest sheet appears to be the base case followed by the increased capacitance and increased voltage cases respectively. At first glance, the case with the lowest pressure may have appeared to be stronger current sheet with its high velocities and plasma current, however, the plasma density Fig. 5.2c and entrained neutral densities Fig. 5.2d correct this assumption. The low pressure case has the advantage of less impedance to the motion of the sheet due to its overall lower neutral densities. This leads to a plasma density nearly three times smaller then the best cases and a smaller entrained neutral density as well for the low pressure case. In the case of increased voltage, we see higher plasma density and entrained neutral density then all other cases, with the increased capacitance case having a higher plasma density then the baseline, but similar entrained neutral densities. The plasma current sheets for all cases seem to form during a period of 0-0.5μs, indicated by an exponential growth in plasma density, with neutrals entrained during this time experiencing ionization collisions rather than charge exchange collisions, becoming absorbed by the current sheet. After this phase is the acceleration phase which continues until the Lorentz and collisional forces balance at around $\sim$1-1.5 μs. During this time the entrained neutral density begins to increase as entrapped neutrals are no longer instantly ionized by or slip past the current sheet. Entrained neutral density continues to rise in a linearly while the plasma density levels off for the rest of the simulation.

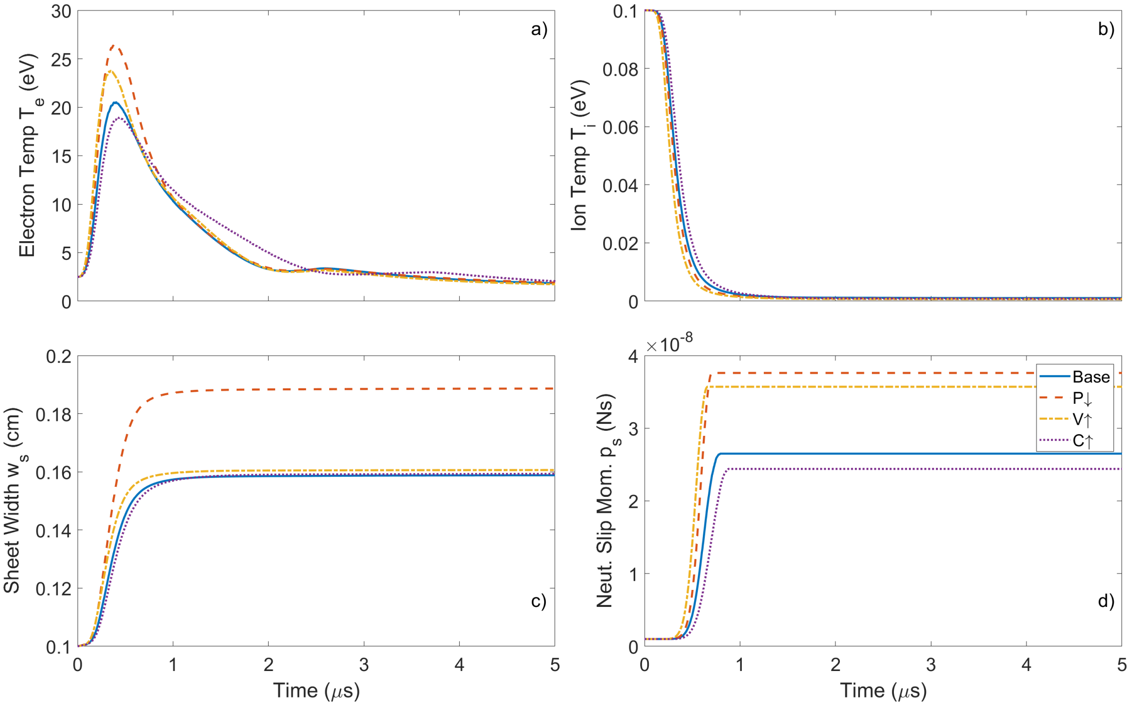

Figure 5.3: Plots of several derived plasma characteristics from the 1-D model for all four cases. Data is generated from the initial conditions presented in Tables 5.2-5.5.

Fig. 5.3 presents the electron and ion temperatures as well as the plasma sheet width and neutral slip moment. In Fig. 5.3a we see the electron temperatures rise due to Ohmic heating before being overtaken by the inelastic losses around 1 μs into the simulation time until reaching an equilibrium. The low pressure cases reached the highest electron temperature at $\sim$27 eV followed by the high voltage and base cases with the high capacitance case reaching the lowest electron temperature. Fig. 5.3b shows a trend of decreasing ion temperatures for all cases which displays the lack of energy coupling into the ion population as expected. Fig. 5.3c displays sheet width and shows how the high velocities of the low pressure case sheet allow for more interactions with the neutral particles, rapidly increasing sheet width compared to the other cases. Finally, Fig. 5.3d shows a larger momentum of slipped neutrals for the low pressure case compared to the other cases further indicating a lack of absorption of neutrals into the current sheet for that case. Here we also see the increased voltage case experience a large momentum of slipped neutrals which is due to the larger current sheet density acting as a slug mass accelerating a larger percentage of neutral particles it comes in contact with.

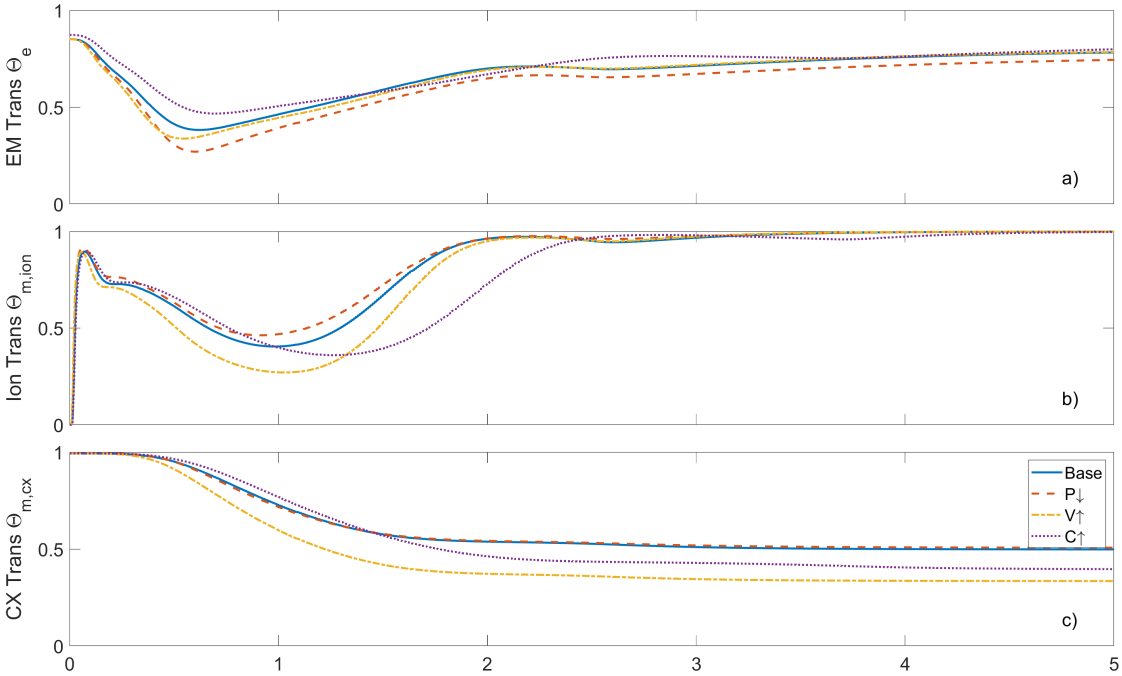

Figure 5.4: Transparency factors for each case generated from the 1-D model. Data is generated from the initial conditions presented in Tables 5.2-5.5.

Fig. 5.4 presents the transparency of the plasma sheet to a) electromagnetic fields, b) mass entrainment due to ionization , as well as c) mass entrainment due to charge exchange collisions for each case. In a) we identify the plasma current sheet for each case has high permeability until ∼0.5 mus into the simulation. From b) and c) we can see a low ionization mass transparency from 0.5-1.5 μs indicates a region of plasma density growth as previously seen, while charge exchange becomes the dominant mass entrainment driver after ∼1.5 s.

The numerical model has given a baseline on what to expect for comparison of the four cases and can now be compared to actual experimentation on the HiPeR-PIT.

5.2 Experimental Results

This section will cover the experimental results from imaging and inter-plasma diagnostics of the HiPeR-PIT for the four cases presented in Table 5.1, beginning with imaging, then measurements from the B-dot probe, Rogowski coil, and Electric field probes respectively.

5.2.1 Current Sheet Imaging

This subsection provides visualization of the current sheets for each case through the use of the Kirana High-speed camera and a DSLR camera. The Kirana allowed for images of the current sheet at 5,000,000 frames per second. Marks were placed on the vacuum chamber in cm increments from the coil face to allow for identification of sheet position and width through observation.

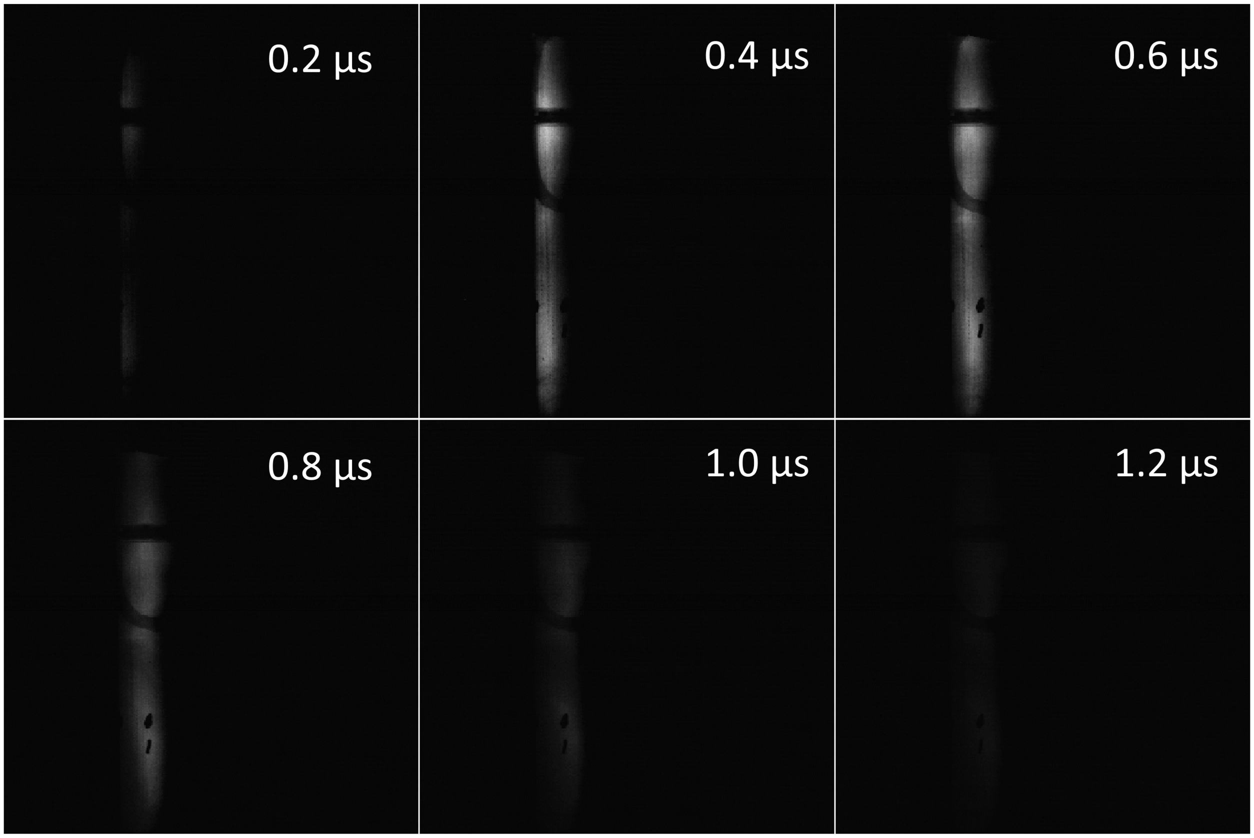

Figure 5.5: Images of the current sheet taken using the Kirana high-speed camera at 5,000,000 frames per second. Images taken represent the baseline case. Images are referenced to a start time of the coil circuit closing. Data is measured at the conditions described in Table 5.1.

Fig. 5.5 shows the current sheets evolution through the first half cycle of the acceleration circuit for the baseline case. The sheet starts to form at 0.2 μs, accelerating until the 0.8 μs mark where the current sheet begins to dissipate and collapse towards a single point at ~1.1 cm from the coil face. By 1.2 μs, the current sheet has completely dissipated. It is important to note that while the sheet appears to become stationary at 0.8 μs, the particles continue on with the same momentum, but the plasma dissipates thus losing any form of visualization of position or particle distribution. Fig. 5.5 provides a baseline of what a clearly defined current sheet which forms on the coil face appears like.

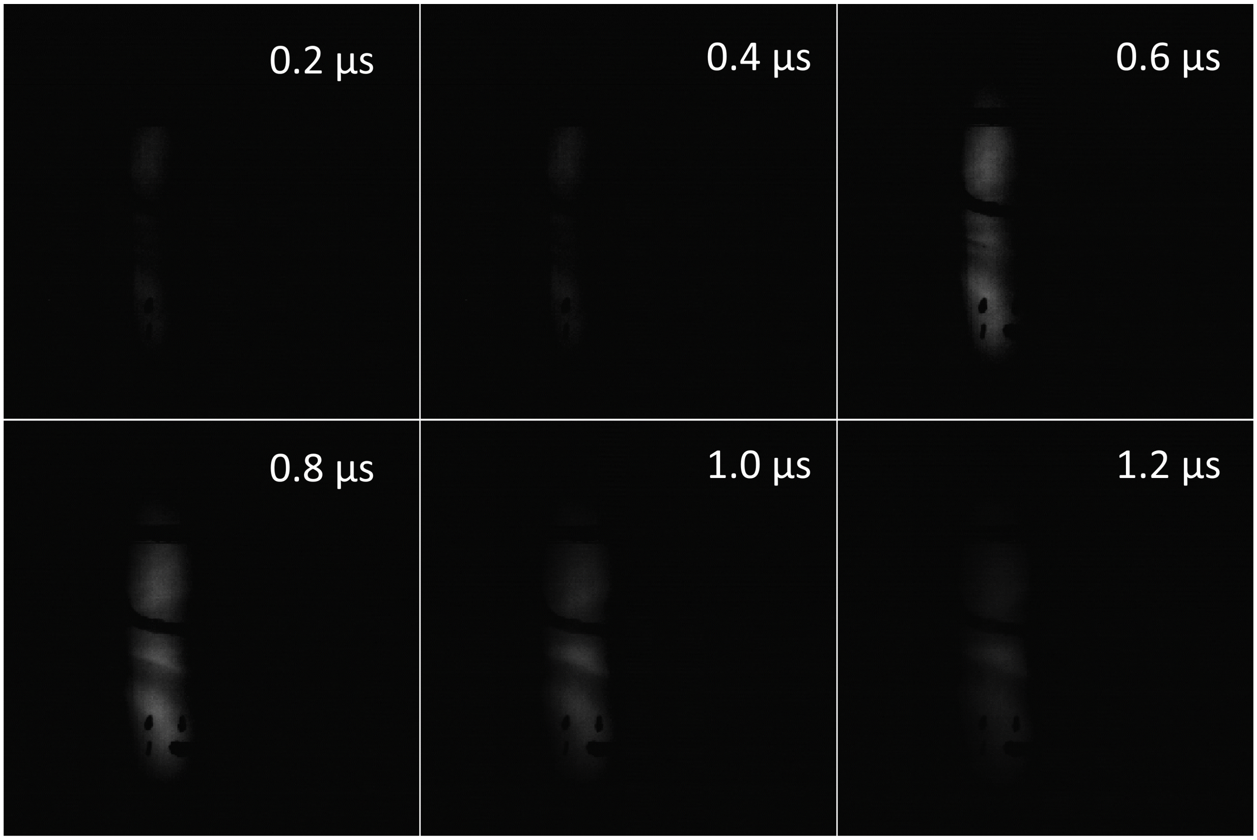

Figure 5.6: Images of the current sheet taken using the Kirana high-speed camera at 5,000,000 frames per second. Images taken represent the low pressure case. Images are referenced to a start time of the coil circuit closing. Data is measured at the conditions described in Table 5.1.

Fig. 5.6 shows the current sheets evolution through the first half cycle of the acceleration circuit for the low pressure case. A plasma plume begins to form at 0.2 μs, growing in width and accelerating until the 1.0 μs mark where the plasma plume begins to dissipate and collapse towards a single point ~1.6 cm from the coil face. By 1.4 μs, the plasma has completely dissipated. In this case, the plasma seen does not take on a plasma current sheet appearance, instead forming a plume of plasma that accelerates from the coil. The shape is not uniform or densely packed in a planar disk as a strong current sheet is expected to appear.

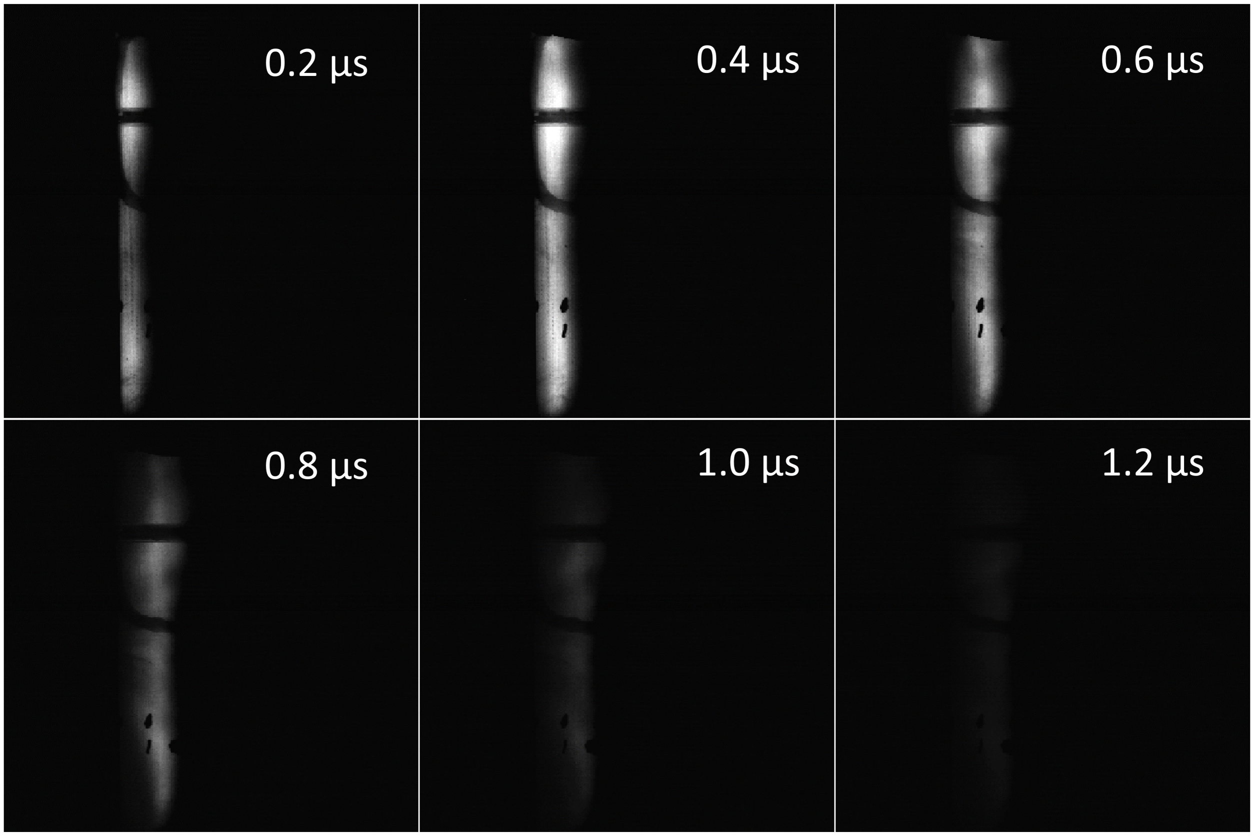

Figure 5.7: Images of the current sheet taken using the Kirana high-speed camera at 5,000,000 frames per second. Images taken represent the high voltage case. Images are referenced to a start time of the coil circuit closing. Data is measured at the conditions described in Table 5.1.

Fig. 5.7 shows the current sheets evolution through the first half cycle of the acceleration circuit for the high voltage case. The sheet starts to form at 0.2 μs, accelerating and gaining significant width until the 0.8 μs mark where the current sheet begins to dissipate and collapse towards a single point at ~1.6 cm from the coil face. At 1.2 μs, the current sheet is still faintly visible. Here we see a much brighter plasma distribution compared to the previous two cases, indicating a more dense, well-ionized plasma.

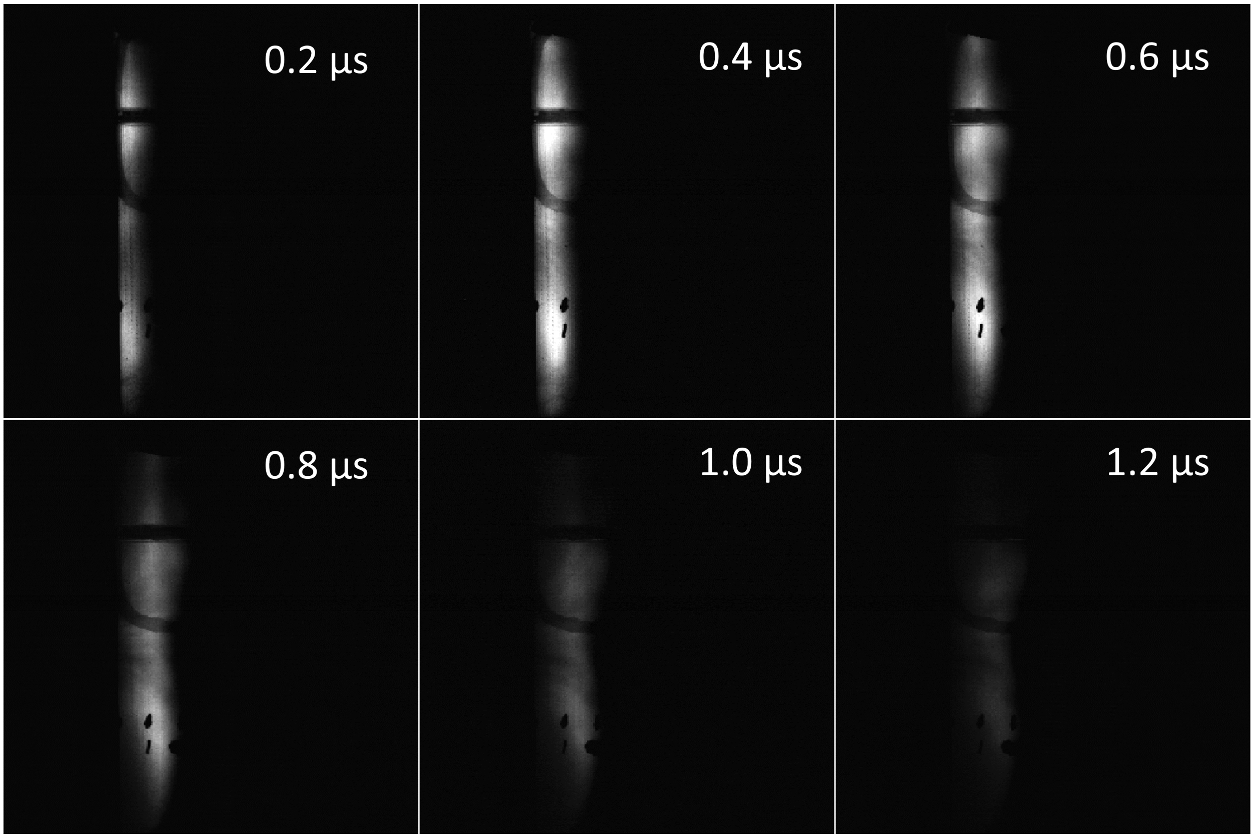

Figure 5.8: Images of the current sheet taken using the Kirana high-speed camera at 5,000,000 frames per second. Images taken represent the high capacitance case. Images are referenced to a start time of the coil circuit closing. Data is measured at the conditions described in Table 5.1.

Fig. 5.8 shows the current sheets evolution through the first half cycle of the acceleration circuit for the high capacitance case. The sheet starts to form at 0.2 μs, accelerating and gaining significant width until the 0.8 μs mark where the current sheet begins to dissipate and collapse towards a single point at ~1.4 cm from the coil face. At 1.2 μs, the current sheet is still visible making this the longest lasting plasma of all the cases which is expected as the frequency of the energy pulse is significantly slower due to the increased capacitance. The plasma appears bright and densely packed similarly to the high voltage case.

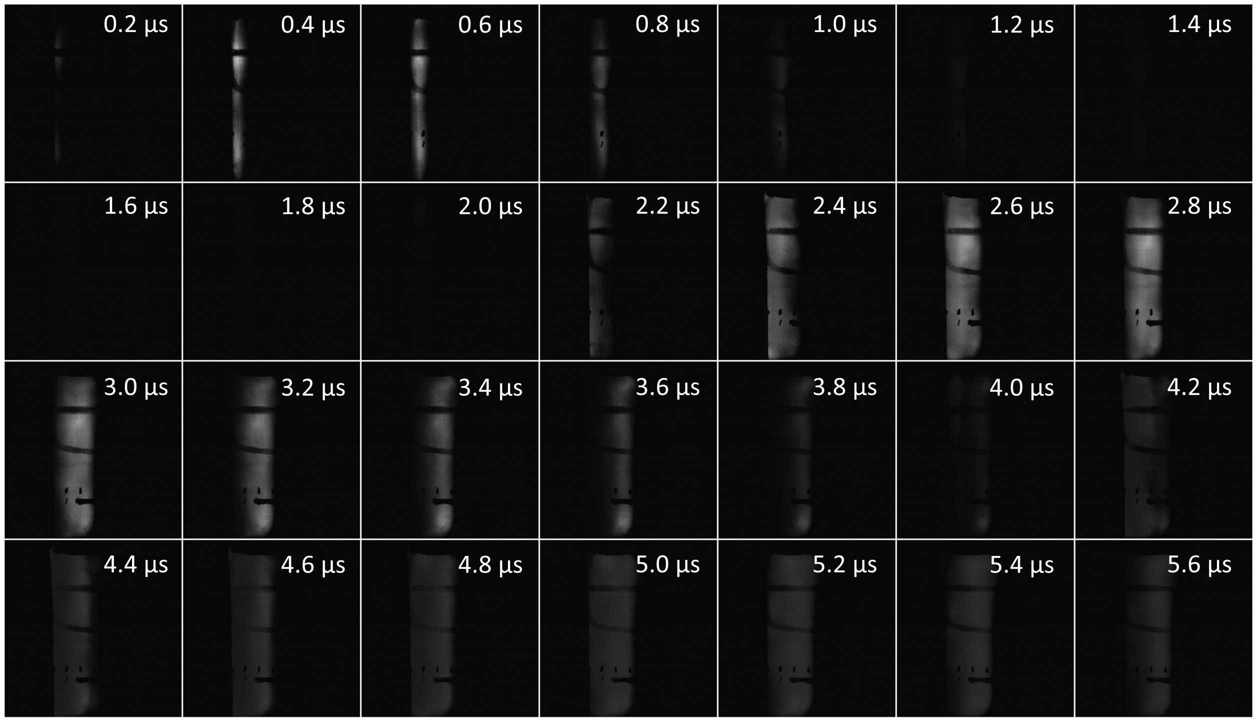

Figure 5.9: Images of the plasma taken using the Kirana high-speed camera at 5,000,000 frames per second. Images taken represent an expanded baseline case featuring multiple plasma entities. Images are referenced to a start time of the coil circuit closing. Data is measured at the conditions described in Table 5.1.

Fig. 5.9 serves as reference for what happens after initial sheet termination using the baseline case as an example. Here we note that the time shown consists with roughly two full cycles of the acceleration circuit discharge. After termination, another plasma entity forms and then terminates in a similar fashion to the previous sheet, forming several different plasma entities until the acceleration coil no longer has the current rise time to form another. These plasma entities after the first initial sheet lose the compact planar current sheet behavior and instead manifest as a multiple cm wide column of plasma that collapses towards the downstream end of the column which in the baseline case was at ∼3 cm. One point of note here is that the visible region of the second sheet expands nearly twice the distance of the initial sheet, which is seen in other cases as well. This may indicate that their is a lack of pre-ionization for the initial current sheet to fully develop, thus allowing for another sheet to form easily in its ionized wake and travel further indicating better coupling then the first sheet. Analysis in this thesis focuses only on the initial current sheet formed in the first cycle, however future analysis can be done on these sheets by performing an axial sweep of the plasma diagnostics.

Analyzing Figures 5.5-5.8 allows for an estimate of the sheet positions and sheet widths as a function of time for each case.

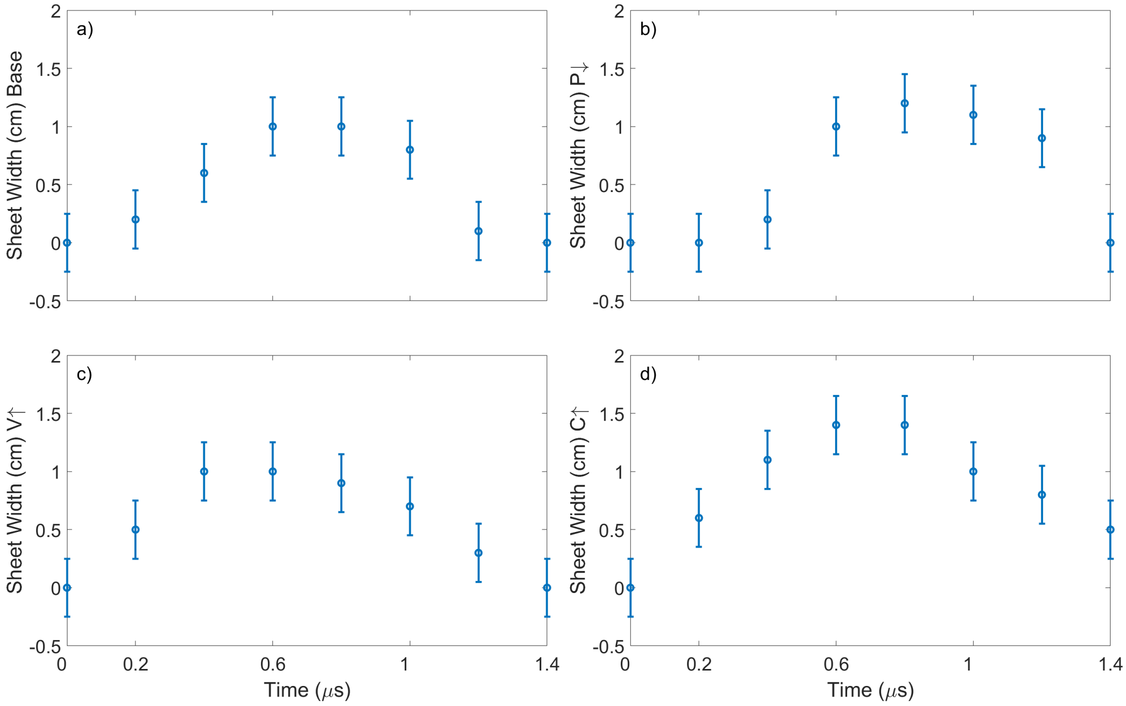

Figure 5.10: Estimates of sheet width using the photos provided from the Kirana. Approximations were made using 1 centimeter markings on the vacuum chamber side as reference. Data is generated from the conditions described in Table 5.1.

As can be seen from Fig. 5.10, the visible plasma sheet width starts at zero until the formation phase of ∼0-0.2 μs and then increases during the acceleration phase of the current sheet, ∼0.2-0.8 μs, before collapsing during the termination phase ∼0.8-1.4 μs. This occurs for all cases and is a similar process to that described by Polzin seen in the FARAD IPPT [26]. The sheet widths presented will be used to form estimates of current density later in the analysis.

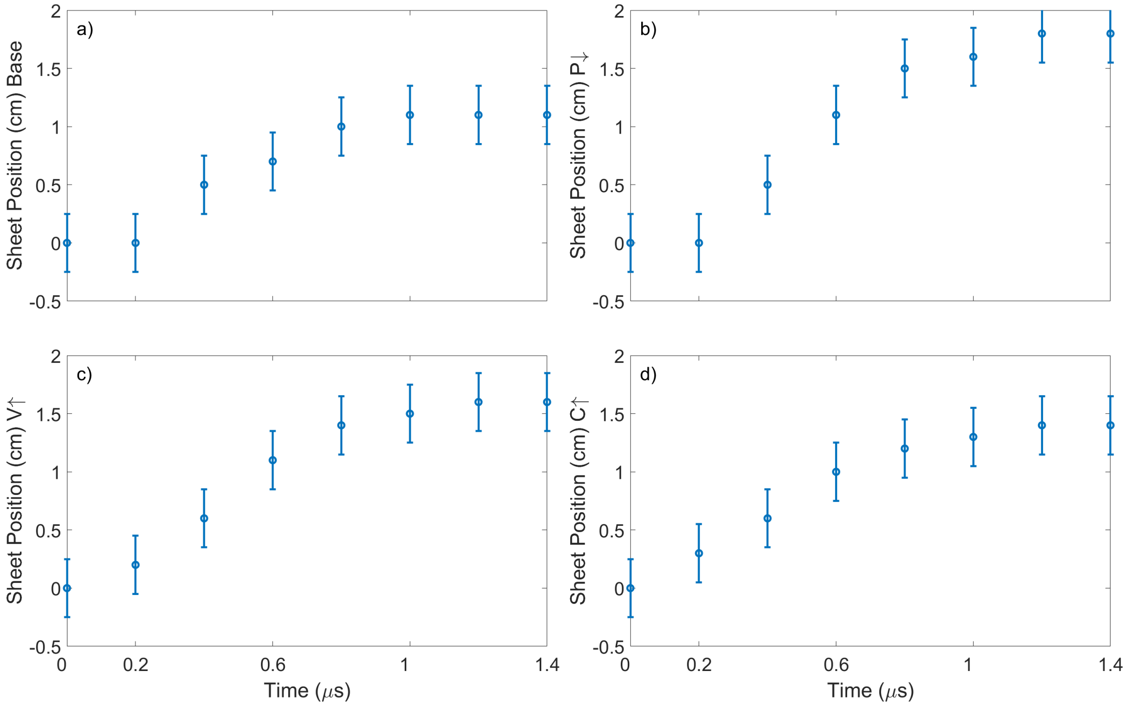

Figure 5.11: Estimates of sheet position using the photos provided from the Kirana. Approximations were made using 1 centimeter markings on the vacuum chamber side as reference. Data is generated from the conditions described in Table 5.1.

Fig. 5.11 presents the visible plasma sheet positions which start at zero until the formation phase of ∼0-0.2 μs and then increases during the acceleration phase of the current sheet, ∼0.2-0.8 μs, before leveling at the last visible locations at ∼0.8-1.4 μs. A behavior of note here is that all plasma entities observed seem to form directly on the face of the coil as desired. Using the position and time data presented in 5.11, we can estimate a maximum velocity of the plasma current sheets ranging from ∼20-25 km/s. with the low pressure case having the fastest moving plasma mass followed by the high voltage and high capacitance cases, with the slowest sheet being the baseline case.

We now move to visualizations of the current sheets from DSLR images. The Rogowski coil and B-dot probe are present in the top portion of the images with the electric field probe down in the bottom section of each image with all probes extending through the plasmas.

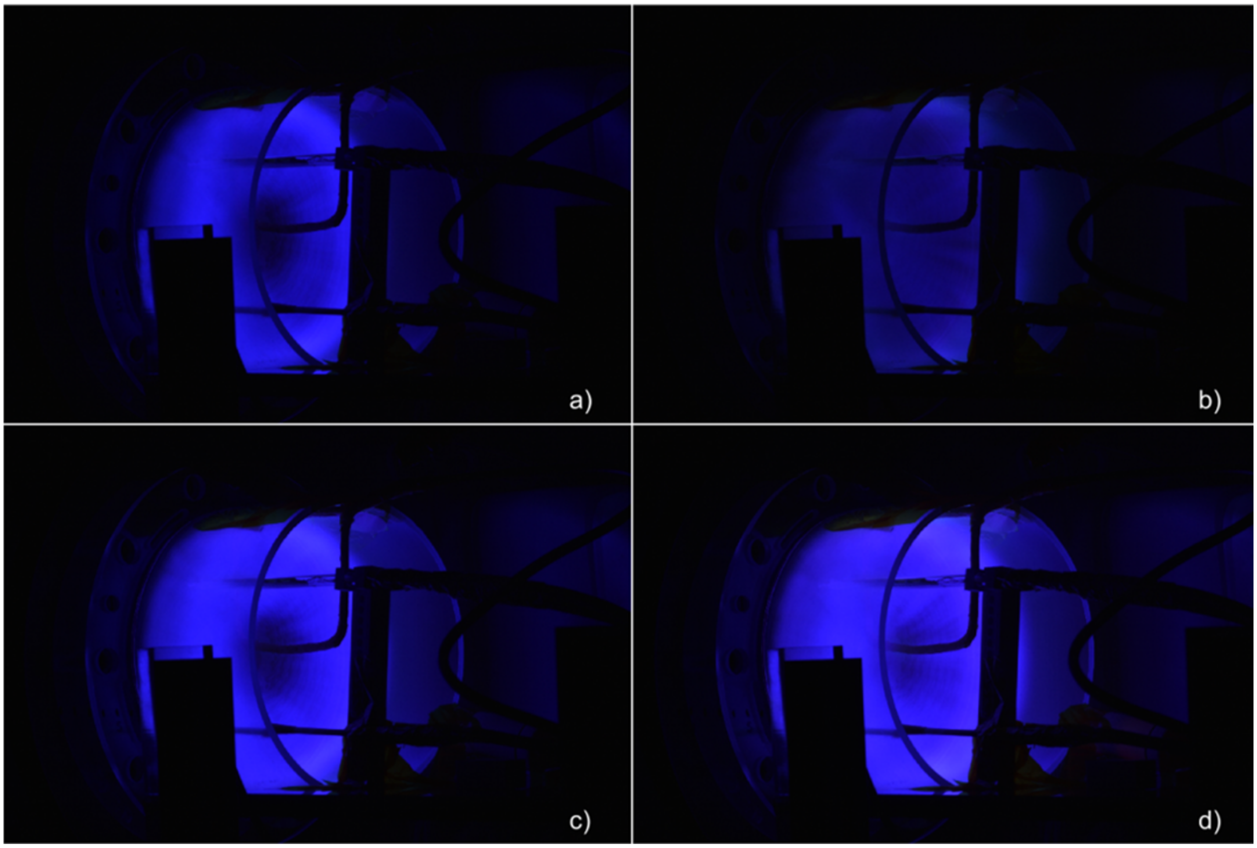

Figure 5.12: DSLR images plasma sheet formation for all cases. a) baseline, b) P↓, c) V↑, and d) C↑. ISO was set to 100 and shutter set to 1/20. Data is measured at the conditions described in Table 5.1.

Fig. 5.12 shows the DSLR images of the plasma for each case over the entire energy pulse of the acceleration coil, ∼20 μs. The first area of note is the annular region that forms in all cases except for the low pressure case shown in Fig. 5.12b. The low intensity hole in the center is an expected behavior of the current sheet as the acceleration coil inner radius starts at 2 cm, thus this region should not contain a dense plasma. Observations of plasma intensity have the high capacitance and voltage cases as the most vibrant plasmas, followed by the baseline case, with the low pressure case having the least vibrant plasma. The plasma in the annular regions appear visually to be more evenly distributed when compared to the low pressure case. Finally, it was observed in all cases that there are dark spoke-like radial regions extending from the plasma center which are believed to be manifestations of the plasma interacting with the radial magnetic fields.

5.2.2 Measured Magnetic Fields

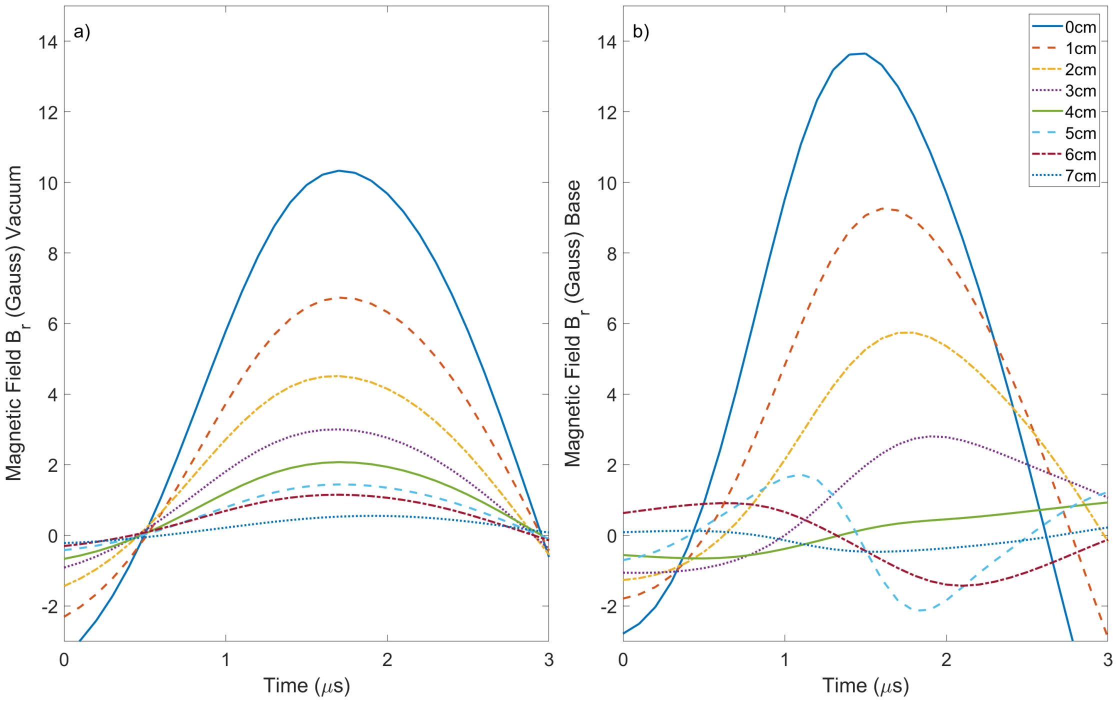

Figure 5.13: Measured magnetic fields for baseline comparing vacuum at baseline conditions to the baseline plasma . B-dot probe measurements captures the radial magnetic fields from 0-7 cm in 1 cm increments. Data is measured at the conditions described in Table 5.1.

Fig. 5.13 presents the measured magnetic field traces for the baseline case in vacuum Fig. 5.13a, and while plasma is present Fig. 5.13b. Here we note that any values other than

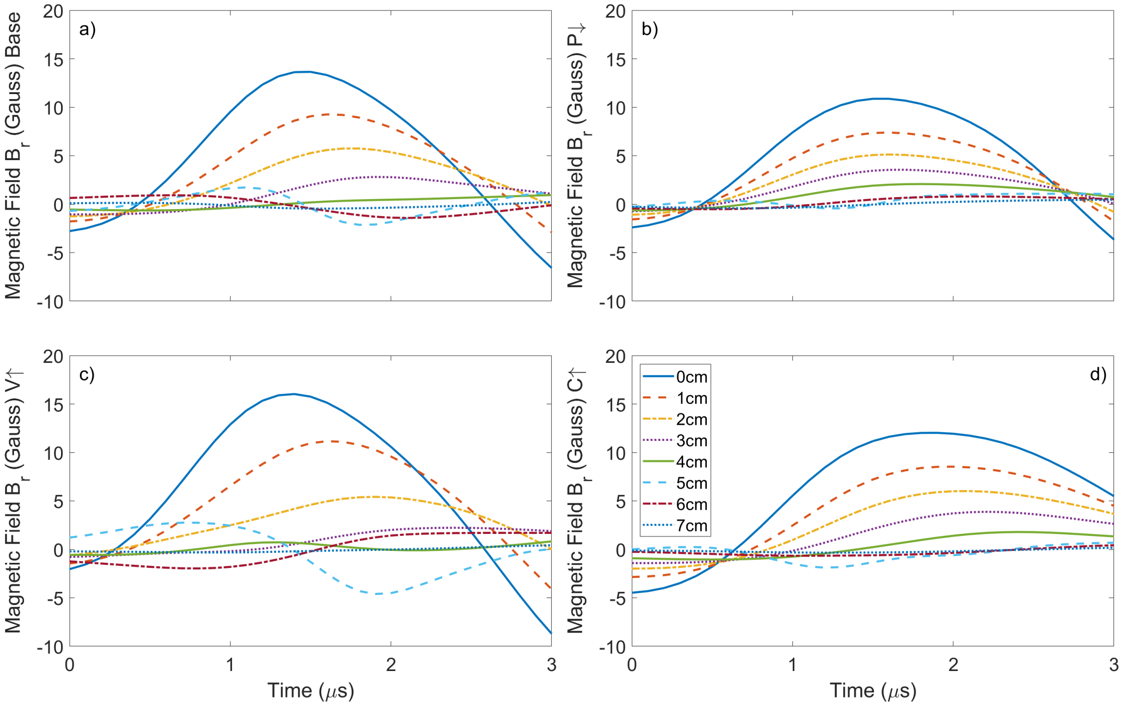

Figure 5.14: Measured magnetic fields for all cases and all probes. B-dot probe measurements captures the radial magnetic fields from 0-7 cm in 1 cm increments. Data is measured at the conditions described in Table 5.1.

zero at the initial time are due to data filtering and numerical integration artifacts. In the vacuum case, phase shift is minimal between all 8 B-dot probe sensors which is true for all cases. The addition of a plasma current sheet as shown in 5.13b, causes phase shift of each subsequent sensor as well as a change in the waveform altogether in the furthest sensors at ~4-7cm which are never directly in plasma. An ideal plasma current sheet which is impermeable to magnetic fields would only show magnetic fields produced by the current sheet downstream from the sheet as the acceleration coil fields would not be able to permeate through. Distortion of the wave forms of the magnetic fields aft of the plasma indicates that while the baseline current sheet isn't completely impermeable to the coil fields, some portion of the field energy is being deposited which indicates that a sheet has indeed formed.

Figure 5.14 presents the measured magnetic field traces for each case for the first cycle. Here we note the phase shift present for each B-dot chip that gets further from the coil face. Waveform distortion and phase shifting of the further B-dot sensors are shown to have an intensity in the order of greatest being the increased voltage case, followed by the base line and increased capacitance cases, with the least distortion seen in the low voltage case. This is another indication that the low voltage case is not forming a current sheet or the current sheet formed is the weakest of all the cases. The coil magnetic fields are detectable through all plasma cases, which indicates that all the sheets are somewhat permeable indicating weak current sheet formation across all cases. Magnetic field traces were repeatable between different current sheet measurements, however alignment of the B-dot probe to the radial magnetic fields was conducive to error of $\sim \pm 5\%$.

5.2.3 Measured Currents

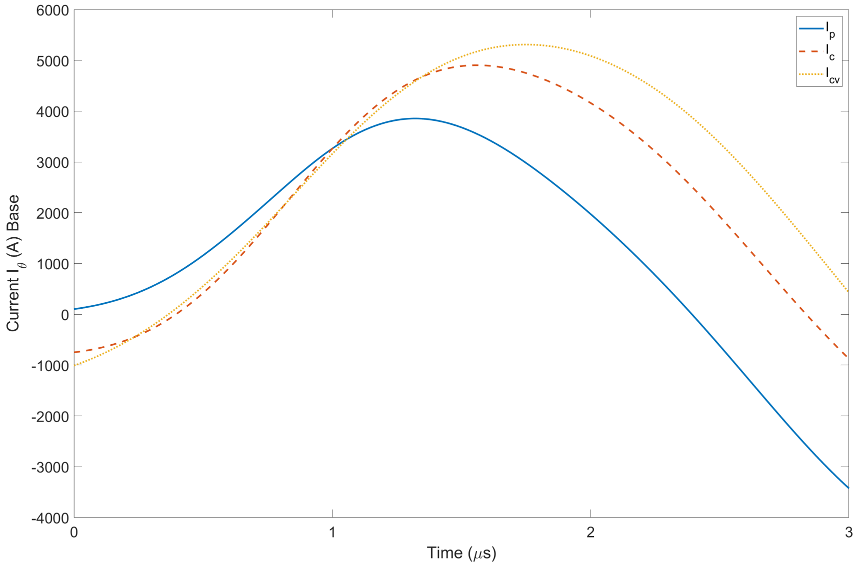

Figure 5.15: Comparison of vacuum shot coil current to measured coil and plasma currents for baseline case. Data is generated from the conditions described in Table 5.1.

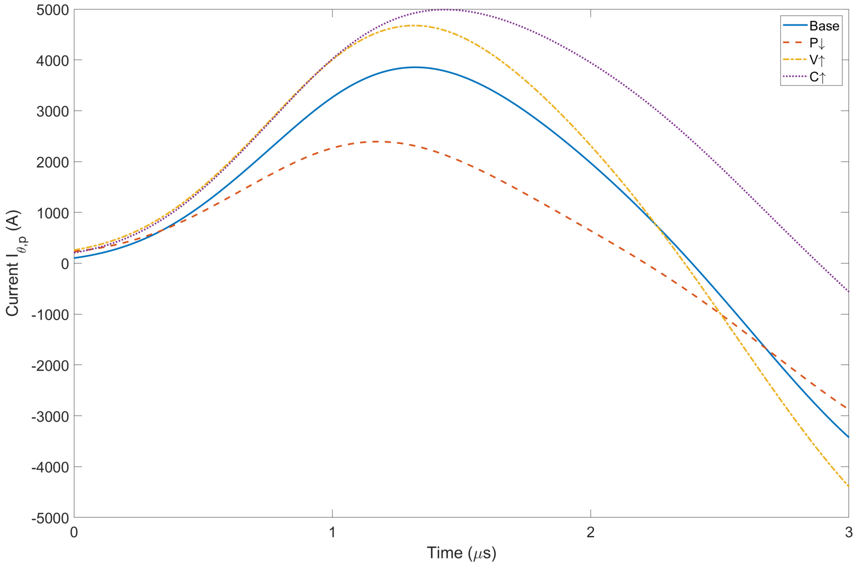

Figure 5.16: Measured plasma currents for all cases. Data is generated from the conditions described in Table 5.1.

Figure 5.15 presents the measured coil and plasma currents for the baseline case as well as the coil current for the baseline case in vacuum. We see significant phase shift between the plasma current, and coil current which is due to the transparency of the current sheet to the electromagnetic fields at formation. Phase shift in the presence of plasma compared to the vacuum case indicates the coil has coupled with the plasma as intended.

Figure 5.16 provides the plasma current traces for the first cycle for all cases. Here we see the cases fall from highest to lowest plasma currents as, the high capacitance case, high voltage case, baseline, and low pressure cases respectively.

Figure 5.17 provides the coil current traces for the first cycle for all cases. Coil currents follow similar trends to the plasma currents, but are higher overall. Current traces were fairly repeatable between pulses with a maximum error of $\sim \pm 5\%$.

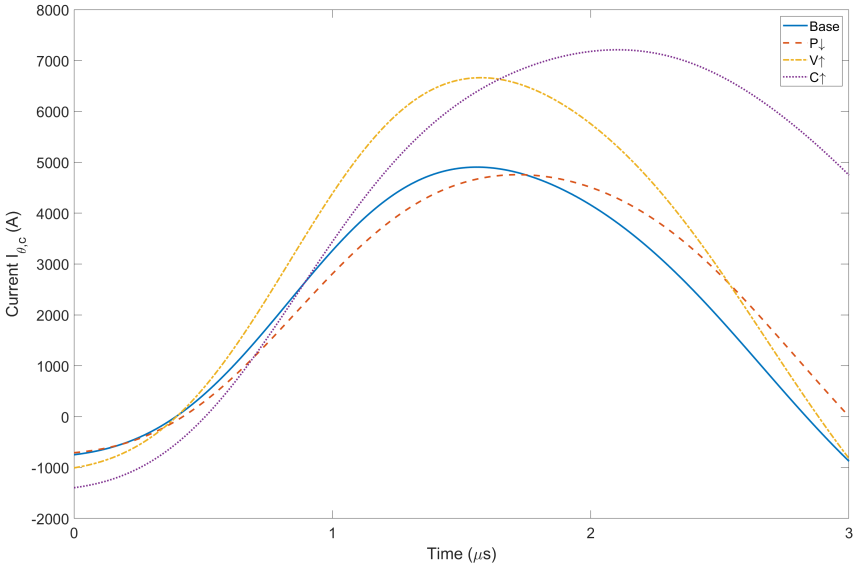

Figure 5.17: Measured coil currents for all cases. Data is generated from the conditions described in Table 5.1.

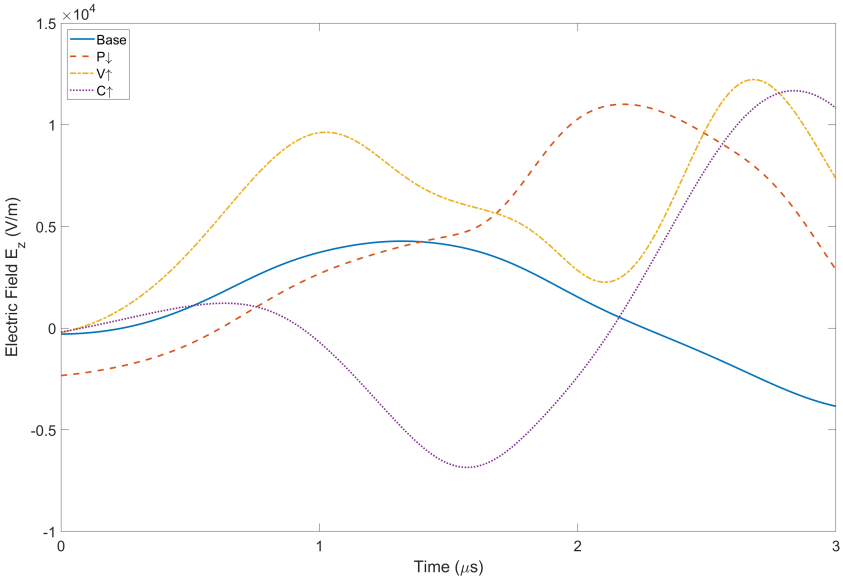

Figure 5.18: Measured Electric Fields for all cases at a position of ∼1.3 cm. Data is generated from the conditions described in Table 5.1.

5.2.4 Measured Electric Field

Figure 5.18 provides the electric field traces for each case measured at a location ∼1.3 cm from the coil face. The electric field traces were mostly positive throughout the entirety the initial energy pulse half cycle with the exception of the case of high capacitance which saw a negative electric field in the region of 1-2μs indicating a reversal of the electric field. This is thought to be due to the current sheet passing the electric field probe during the specified time period. The electric field measurements are highly dependent on the position of the probe and require a sweep of the axial direction to get a complete picture of the electric fields as they evolve with the plasma current sheet. Measurements from the electric field probe were also found to vary significantly from pulse to pulse. Due to the variability and inability to calibrate the probe against a known electric field, uncertainty from electric field measurements was taken at ±20%.

5.2.5 Sheet Plasma Density Calculation

With results of the azimuthal current, radial magnetic fields, and axial electric fields, as well as current sheet width estimates found in Fig. 5.10, an estimate of the plasma sheet density can be made for each of the cases using Eq. 4.11. For the calculation, the point in each case where the plasma current is maximum was used as a reference point which typically occurs at ∼1.5-2 μs.

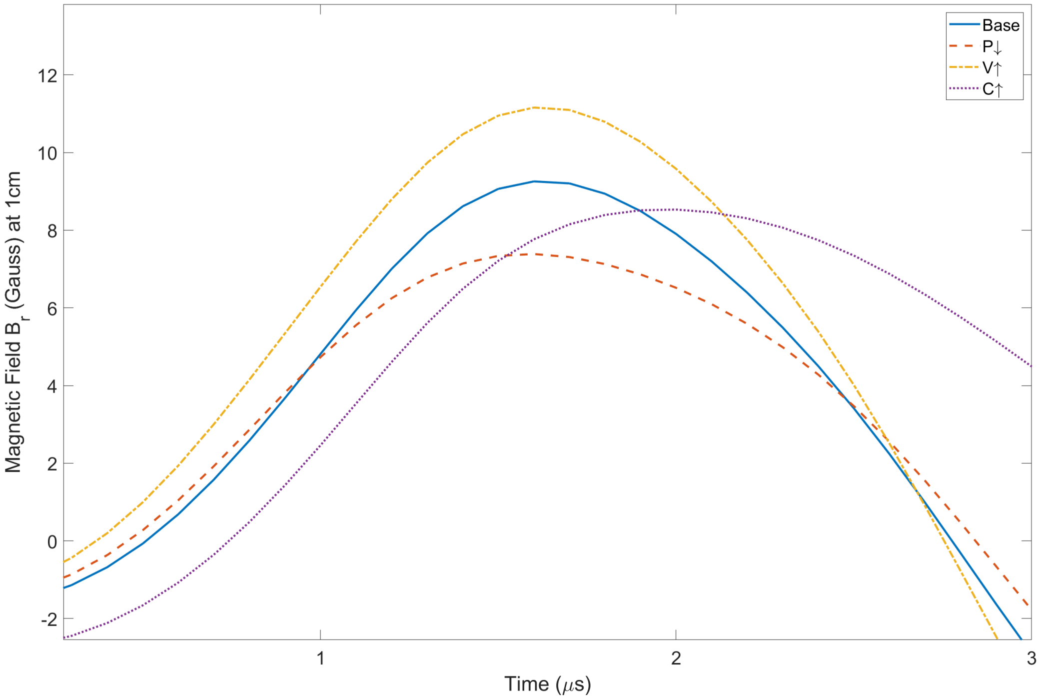

Figure 5.19: Measured magnetic fields for all cases at 1 cm. This probe sensor was used for plasma density measurements. Data is measured at the conditions described in Table 5.1.

Figure 5.19 shows the magnetic field traces used for the plasma density measurements for each case. The time of maximum current was used to get the magnetic and electric fields at that moment for all cases.

Table 5.6: Plasma current sheet density estimates using sheet width, Rogowski Coil, E-field probe, and B-dot probe calculations at peak current. Estimates are derived from measurements taken at conditions described in 5.1

Case	Plasma Density
Base	7.4±2.2e18 m^{-3}
P↓	4.1±1.2e18 m^{-3}
V↑	2.1±0.6e19 m^{-3}
C↑	1.2±0.4e19 m^{-3}

Plasma density estimations at peak current are presented in Table 5.6 for each case. It is important to note that these are merely rough estimates and we can only pull generalized trends from this calculation, a more in depth calculation using a full axial sweep of the electric field probe is required for more accurate estimates. From these plasma density calculations, we can form an idea of how the current sheet appears at peak plasma current with the low pressure case having the lowest density, followed by the baseline, and finally the high capacitance and high voltage cases respectively. With this final estimate, it seems that both the high voltage and high capacitance cases provide the highest density current sheets, followed by the baseline case producing a less dense current sheet. The low pressure case appears to be a different mode of operation for a low energy IPPT which produces a low density, permeable mass of plasma.

5.3 Discussion

5.3.1 Comparison of Numerical and Experimental Results

Before comparing the numerical model and experimental results it is relevant to cover some underlying assumptions the model makes which are described in detail by Little et al. [13], and McCulloh [19]. The first assumption is that plasma sheet properties are assumed to be uniform within the volume of the plasma which diverges from literature on the subject [6]. Another pertinent assumption is the absence of modeling recombination reactions as well as radial expansion and cooling. Comparing the numerical and experimental measurements from the HiPeR-PIT provide several key differences. One error source of note in regards to chamber pressure was the gas injection mechanism, which consisted of two needle valves. Minor adjustments to the valves could vary the chamber pressure by ∼0.5 mTorr and the chamber pressure would sometimes vary from the initial setting with time. Another source of differences between experimentation and the model could derive from the pre-ionization percentage assumed or the initial electron temperature. Two sources of pre-ionization were used in this experiment, however the distribution and percentage of pre-ionized particles at the coil face were unknown. Initial electron temperature was taken from previous literature where more diagnostics were available [26].

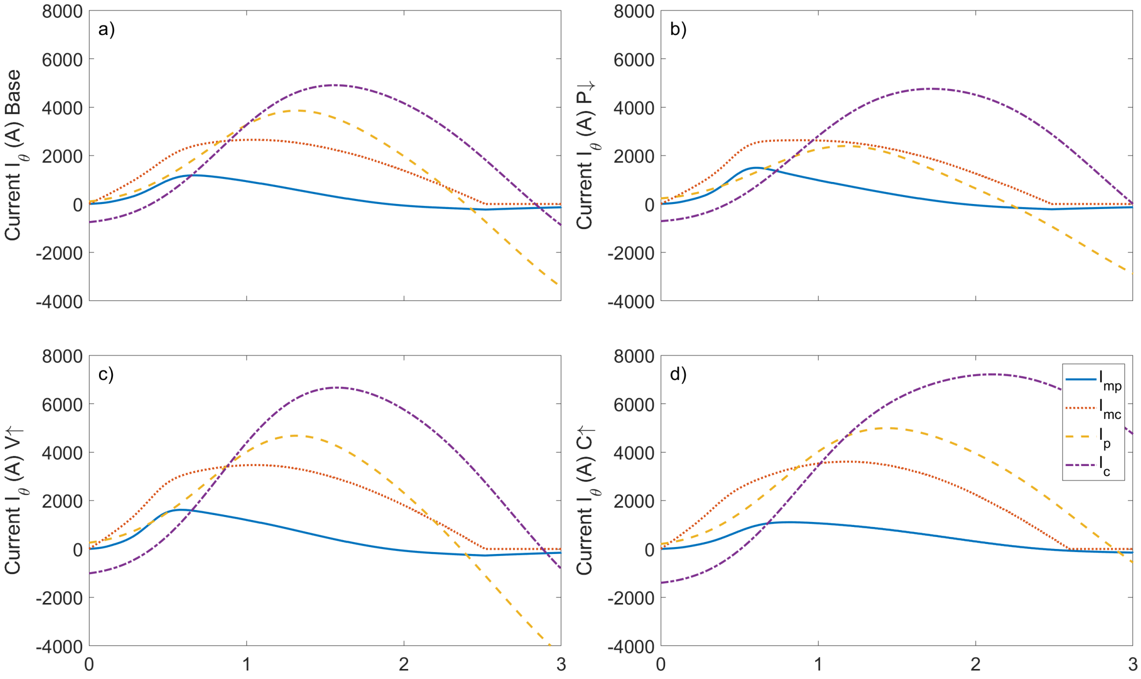

Figure 5.20: Measured and numerical plasma and coil currents for all cases. Data is generated from the conditions described in Table 5.1.

Finally comparing the coil and plasma current traces from numerical to experimental as shown in Fig. 5.20 shows a large discrepancy for all cases. It would be ideal to place a current transformer directly on the coil positive lead to confirm the Rogowski coil reading for verification of the larger currents.

Simulation of the current sheet position and velocity in the model match particularly well as can be seen in Fig. 5.21. All early velocities seem to match closely amongst the cases as be seen from the slopes of the displacement lines, and sheet positioning follows the general trend with the highest deviation seen in the low pressure case. Towards the end of the experimental plasma current sheet visible life cycle is where divergence of sheet positioning and other associated characteristics occur.

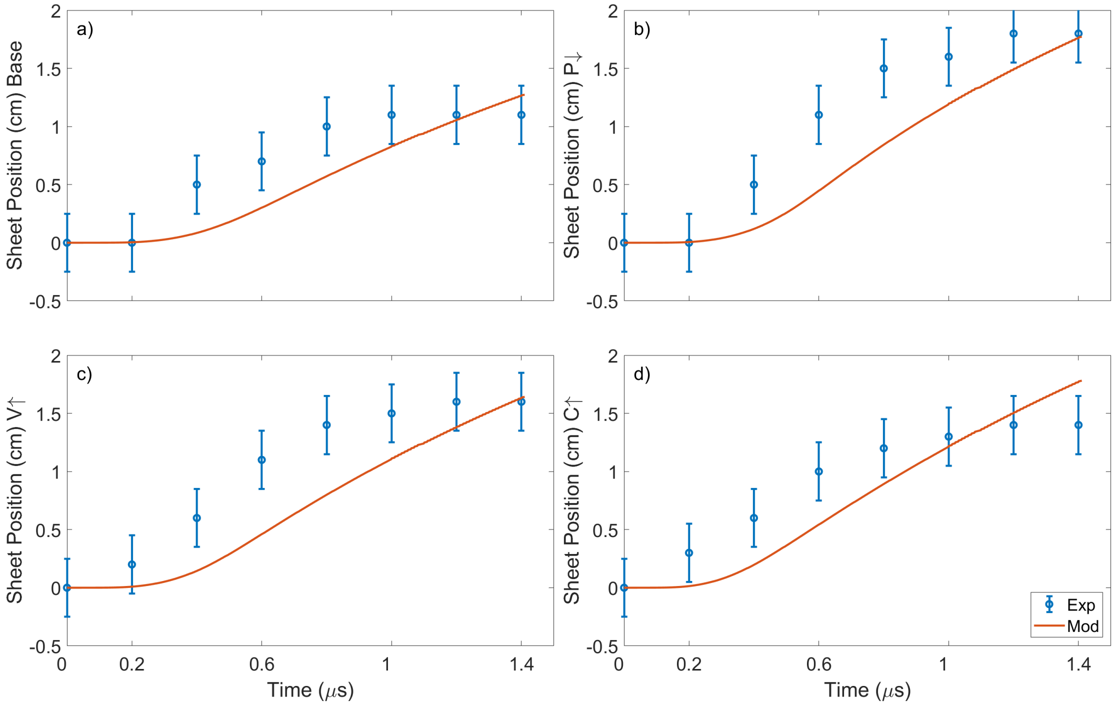

Figure 5.21: Comparison of visualized sheet position to the numerical model. Data is generated from the conditions described in Table 5.1.

Other areas of agreement with the numerical model lay within the general trends seen in each case. The model indicates the lowest plasma densities are seen in the lower pressure case Fig. 5.2c while the other cases experience higher densities, particularly cases of increased energy shown in Table 5.6. Total number densities estimated are over an order of magnitude less then the model which indicates weak sheet formation due to permeability of the current sheets for all cases. The model does agree with an overall indication that the best cases for sheet formation are the cases of increased capacitance and increased voltage. Increased voltage and main bank capacitance were expected to increase current sheet formation as both methods add energy into the system thus directly increasing total current and current rise time, which directly influences current sheet formation. Energy of the HiPeR-PIT is currently limited by the switch voltage capabilities in the discharge circuit.

An increase of the HiPeR-PIT energy to ∼8 J/pulse corresponding with a main bank charge of 3kV and PI bank charge of 3kV would be ideal. This would allow for stronger pre-ionzation and more energy to be deposited into the current sheet during formation phase near the coil face.

More insight into potential paths of improvement are gained from observations between the baseline and low pressure case. Lack of planar current sheet formation in the low pressure case indicates the need to increase the initial neutral gas density of the HiPeR-PIT past some critical density for a given energy condition in order to form an annular planar current sheet following the shape of the coil. The minimum pressure at which annular current sheets seemed to form in the HiPeR-PIT approaches ∼4.5 mTorr, which reached the limit of the current vacuum chamber pumping capabilities. Several experiments were run at lower pressures with a total range of ∼2-4.5 mTorr, which were not analyzed outside of visualization, but none of these tests seemed to produce a sheet-like manifestation in imaging until reaching the higher pressure limit.

5.4 Summary of Findings

An exploratory analysis of the plasma formation in the HiPeR-PIT was conducted to provide insight into potential optimal regimes of current sheet formation for the present experimental configuration. We found that increasing the energy of the acceleration coil pulse resulted in stronger current sheets. It was also identified that decreasing pressure resulted in weaker current sheet formations relative to the other analyzed cases. From analysis of the experimental and numerical results, we find the following in regards to the HiPeR-PIT:

- The model overestimates densities of the current sheets which indicates weak sheet formation, permeability to electromagnetic fields and neutrals, for all cases.

- Several current sheet-like entities form after the initial current sheet and travel further downstream which may indicate lack of proper pre-ionization.

- Increasing the energy output of the HiPeR-PIT to ~8 J/pulse would allow for greater pre-ionzation from the 2nd stage PI potentially allowing for a stronger current sheet formation at the coil face.

- There is a backfill pressure regime, or initial neutral density $n_{n,0}$, where a strong current sheet can form for a given energy. For the baseline case, this is hypothesized to be at ~5-6 mTorr. At higher energies, the backfill pressure should be set even higher.

Chapter 6

CONCLUSION

In this thesis we have presented an analysis on the current sheet formations of the HiPeR-PIT, a planar IPPT with a two-stage pre-ionization scheme. Having two-stage PI allows for total energy discharges at energies much lower than previous IPPT designs in literature [5]. Two studies were performed in this thesis, with the first comprising of the analysis of a one dimensional numerical model of the thruster. The model was used to form a baseline on expected behavior of several current sheet characteristics for different experimental cases. It provided insight into the current sheet formation process and the time-evolution of the current sheet.

The second study performed was the experimental analysis of the current sheet formation through the use of several plasma diagnostics. This study sought to provide an informed direction of what conditions can provide the strongest current sheet formations. Plasma parameters were explored through the use of invasive plasma diagnostics including a Rogowski coil, B-dot probe, and electric field probe, while non invasive diagnostics included a high-speed camera and DSLR for sheet visualization. Both studies were compared to provide an estimation of the present thruster configurations ability to form a strong current sheet.

The HiPeR-PIT is still far from implementation as a real thruster, thus the purpose of this experiment was to evaluate current sheet formation at various test cases to identify the best conditions for a deeper future analysis of thruster performance. The results of the two studies will be briefly mentioned in this chapter along with suggested future development for the HiPeR-PIT.

6.1 Summary of Numerical Results

The results of the numerical model are summarized below for each of the four cases tested.

- Electron temperatures provided insight into the formation process of the current sheet with Ohmic heating dominating during the formation and acceleration process while inelastic losses dominated outside the coupling range of the acceleration coil.

- In the case of a low pressure, the simulated current sheet was able to achieve higher velocities due to a lower plasma density leading to lower collisional drag forces on the current sheet.

- Both the cases of increased voltage and increased capacitance representing increased energies seemed to perform best in the model with the highest plasma densities reached during the life of the current sheet. The high voltage case also had the highest entrained neutral density.

- The baseline case performed slightly worse then the increased energy cases, with the low pressure case having the lowest plasma density and the lowest entrained neutral density.

6.2 Summary of Experimental Results

Analysis of the plasma diagnostics allowed for the following summary of current sheet formations at the cases studied.

- High-speed imaging of the different cases showed a nearly uniform planar sheet form for the baseline and high energy cases, while the low pressure case formed a non-uniform plasma plume. Plasma formed directly over the coil face in all cases. Sheets formed on later half cycles as well and traveled further and for longer then the initial sheets before dissipating.

- DSLR photos over the life of the plasma indicated an annular current sheet had formed in all cases except for the decreased pressure case, with the most vibrant plasmas being the higher energy cases.

- Rogowski coil measurements provided both coil and plasma currents that were higher than those seen presented by the model indicating either overall decreased circuit inductance when coupled with the plasma, or potential error.

- B-dot probe measurements indicated plasma current sheet formation through distortions and phase shift in the wave forms of each successive probe location. The low pressure case had the lowest amount of distortion in the B-dot probe indicating high electromagnetic transparency of the plasma sheet.

- Electric field measurements produced a mostly positive electric field with the high capacitance case producing a negative electric field indicating a possible field reversal.

- Plasma density estimates for the four cases indicated the highest sheet densities occur for the increased energy cases while the low pressure case had the lowest estimated plasma density. Comparison with plasma densities obtained from the model indicate weak current sheet formation for all cases.

- Experimental results thus indicate moving towards higher energies at higher propellant injection pressures for stronger current sheet formation.

6.3 Future HiPeR-PIT Development

Experimentation on the present HiPeR-PIT has illuminated several potential optimizations that can be tested to attempt to increase thruster performance and improve the testing apparatus. These changes will require extensive testing to validate their benefits to current sheet formation and overall efficiencies.

The first potential optimization would be an increase in propellant pressure as discussed previously. This would require an upgrade of the current turbo pump and roughing pump setup to deal with the higher gas flow. On the subject of gas flow, implementation of flow meters rather than needle valves would contribute to certainty of backfill pressures and repeatability of pressure based conditions.

The second optimization pertains to energy per pulse of the HiPeR-PIT. The coil design was made to operate at energies of roughly ∼8 J/pulse, however due to limitations due to the IGBT switches used, energies of only ∼3.5 J/pulse can be achieved in the current configuration. Switches capable of ∼6 kV must be implemented to be able test higher energy pulses.

The last potential optimization would be in pre-ionization of the thruster propellant. The first stage RF pre-ionization scheme presented several challenges throughout the design of the current HiPeR-PIT configuration. Initially the RF was located at the center of the HiPeR-Pit, but it was found to couple into the acceleration coil preventing any ionization of the injected gas. The RF was thus moved inside the chamber downstream of the acceleration coil, however this setup would not be incorporated into an actual thruster design. While inside the chamber, some of the RF energy seems to couple into the plasma diagnostics, specifically the Rogowski coil, but operating at 100 W allows for a background plasma. Potential optimizations would see the RF near the face of the thruster, similar to a cathode of traditional hall thrusters, or the removal of the RF coil altogether. Other potential pre-ionization options include running the RF directly through the acceleration coil, or the implementation of an m=1 coil [3], positioned directly around the gas injection plane. Any change to the pre-ionization scheme would require extensive testing to verify improvement of the of the initial ionized particle density and uniform distribution.

BIBLIOGRAPHY

[1] S. Bose, M. Kaur, K. Barada, J. Ghosh, P. Chattopadhyay, and R. Pal. *Understanding the working of a B-dot probe. European Journal of Physics. J. Phys.*, 40(015803), 2019.

[2] E. Choueiri and K. Polzin. *J. Propuls. Power*, 22(3), 2013.

[3] H. Conrads and M. Schmidt. *Plasma Sources. Sci. Technol.*, 9(441), 2007.

[4] C. L. Dailey. *Investigation of Plasma Rotation in a Pulsed Inductive Accelerator. AIAA Journal*, 7(1), 1969.

[5] C. L. Dailey and R. H. Lovberg. *The PIT MkV pulsed inductive thruster.* Technical Report NASA-CR-191155, TRW Systems Group, Redondo, CA, 1993.

[6] C. L. Dailey and R. H. Lovberg. *Current sheet structure in an inductive-impulsive plasma accelerator. AIAA*, 10(2)(125), Feb. 1972.

[7] R. Frisbee and I. Mikellides. *The Nuclear-Electric Pulsed Inductve Thruster (NuPIT): Mission Analysis for Prometheus. AIAA*, (3892), 2005.

[8] D. M. Goebel and I. Katz. *Fundamentals of electric propulsion:ion and Hall thrusters.* John Wiley & Sons, 2005.

[9] R. J. Goldston and P. H. Rutherford. *Introduction to Plasma Physics.* Bristol, UK, 1 edition, 1995.

[10] R. G. Jahn. *Physics of Electric Propulsion.* McGraw-Hill, New York, 1968.

[11] M. A. Lieberman and A. J. Lichtenberg. *Principles of plasma discharges and materials processing.* John Wiley & Sons, 2005.

[12] M. Lindero-Hernandez, A. Espino-Hernandez, and M. Romero-Bastida. *Design and construction of a single-axis, low-frequency magnetic probe (B-dot probe) calibrated with a LVvar Helmholtz resonant circuit. Revista Mexicana de Fisica*, 65, 2019.

[13] J. Little, G. McCulloh, and C. Marsh. *Ionization and current sheet formation in inductive pulsed plasma thrusters. In Review*, 2022.

[14] R. Lovberg. *Inference of Plasma Parameters from Measurement of E and B fields in a Coaxial Accelerator. The Physics of Fluids*, 7(S57), 1964.

[15] R. Lovberg and C. Dailey. *AIAA Journal*, 20(971), 1982.

[16] R. H. Lovberg and C. L. Dailey. *A PIT Primer.* Technical Report 005, RLD Associates, Encino, CA, 1994.

[17] A. Martin. *Journal of Physics D: Applied Physics*, 49(025201), 2015.

[18] A. Martin and R. Eskridge. *Journal of Physics D: Applied Physics*, 38(4168), 2005.

[19] Gordon I. McCulloh. *Impact of Neutral Backfill on Plasma Sheet Dynamics in Pulsed Inductive Thrusters.* Master's thesis, University of Washington, Seattle, WA, 2022.

[20] R. Pahl, J. Rovey, and D. Pommerenke. *CALIBRATION OF MAGNETIC FIELD PROBES AT RELEVANT MAGNITUDES. Missouri University of Science and Technology*, 2013.

[21] F. Poehlmann, N. Gascon, and M. Cappelli. *The Deflagration - Detonation Transition in Gas-Fed Pulsed Plasma Accelerators. 43rd AIAA/ASME/SAE/ASEE Joint Propulsion Conference & Exhibit*, (10.2514/6.2007-5263), 2007.

[22] K. Polzin, J. Little A. Martin, C. Promislow, B. Jorns, and J. Woods. *State-of-the-Art and Advancement Paths for Inductive Pulsed Plasma Thrusters. Aerospace*, 7(105), 2020.

[23] K. Polzin, C. Hill, P. Turchi, R. Burton, S. Messer, R. Lovberg, and A. Hallock. *Recommended Practice for Use of Inductive Magnetic Field Probes in Electric Propulsion Testing. Journal of Propulsion and Power*, 33(3), 2017.

[24] K. A. Polzin and E. Y. Choueiri. *IEEE Transactions on Plasma Science*, 34(945), 2006.

[25] K. A. Polzin, K. Sankaran, A. Ritchie, and J. Reneau. *Journal of Physics D: Applied Physics*, 46(475201), 2013.

[26] Kurt A. Polzin. *Faraday Accelerator with Radio-frequency Assisted Discharge (FARAD).* Phd thesis, Department of Mechanical and Aerospace Engineering, Princeton Univ., Princeton, NJ, 2006.

[27] C. Promislow and J. Little. *Operation and Performance of a Power Processing Unit for Inductive Pulsed Plasma Thrusters Operating at High Repetition Rates. In Review.*

[28] P. Saetang and A. Suksri. *The Design and Optimization of Combined Rogowski Coil Based on Printed Circuit Board. EDP Sciences*, 70(10014), 2016.

[29] P. K. Srivastava. *A dipole probe for electric field measurements in the LVPD. Meas. Sci. Technol.*, 27(015902), 2016.

Appendix A

WHERE TO FIND THE 1-D IPPT MODEL

Code for the 1D single-pulse IPPT model with neutral back-fill used in this thesis was developed in Wolfram Mathematica. This code can be found on the authors GitHub page:

- https://github.com/Cameron-W-M/IPPT_Model

The code was developed by Professor Justin Little and PhD candidate Curtis Promislow of the University of Washington Space Propulsion and Advanced Concepts Engineering (SPACE) Lab.

Appendix B

ADDITIONAL KIRANA FOOTAGE

Chapter 5 contains a detailed analysis of the Kirana imaging for the initial current sheet formation of each case studied. In this appendix, we add additional Kirana imaging which includes the first full discharge cycle of the acceleration circuit for cases other than the baseline. These results allow us to compare the plasma formations for all cases in direct comparison to the extended Baseline Kirana footage seen in Fig. 5.9.

In Fig. B.1 we see the first full cycle of the discharge for the low pressure case. Here we note that the initial plasma plume dissipates early as previously noted, however the second plasma plume travels further dissipating at ∼5 cm from the acceleration coil face. This is the furthest traveled plasma of all the cases, however it does not exhibit current sheet characteristics like the other cases.

In Fig. B.2 we see the first full cycle of discharge for the increased voltage case. The secondary sheet which forms at 2.2 μs shows a higher intensity then the baseline case and other cases. The initial sheet which dissipates at ∼1 μs provides an initial wave of ionization which allows for this secondary sheet to couple well with the acceleration coil on the second half cycle. The secondary sheet also travels further than the initial sheet in this case with a total distance of ∼3.5 cm.

Finally in Fig. B.3, we can see the first full cycle of discharge for the increased capacitance case. Similar to the previous cases we see the secondary sheet form. Here the intensity of the secondary sheet is less than that of the high voltage case, however this sheet travels further dissipating at ∼4 cm. Of all cases presented, plasma intensity appeared to be the highest in Fig. B.2, further indicating that the increased voltage case provided the most ideal current sheet.

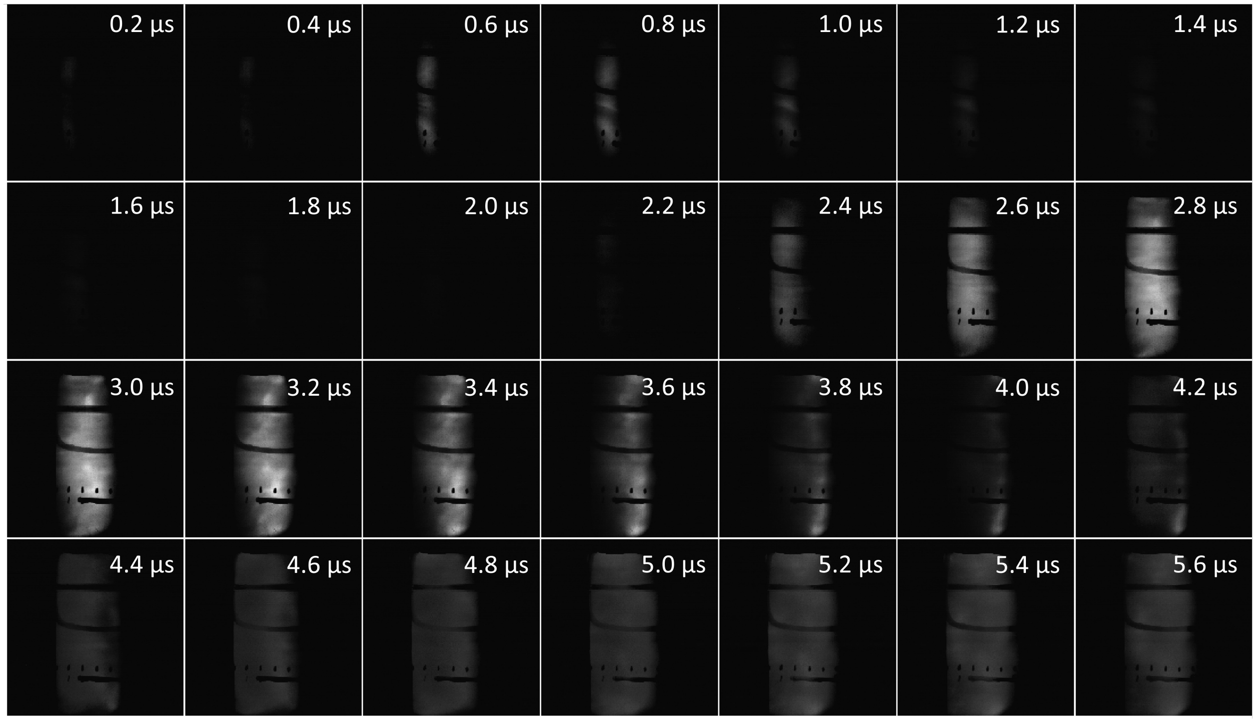

Figure B.1: Images of the plasma taken using the Kirana high-speed camera at 5,000,000 frames per second. Images taken represent an expanded decreased pressure case featuring multiple plasma entities. Images are referenced to a start time of the coil circuit closing. Data is measured at the conditions described in Table 5.1.

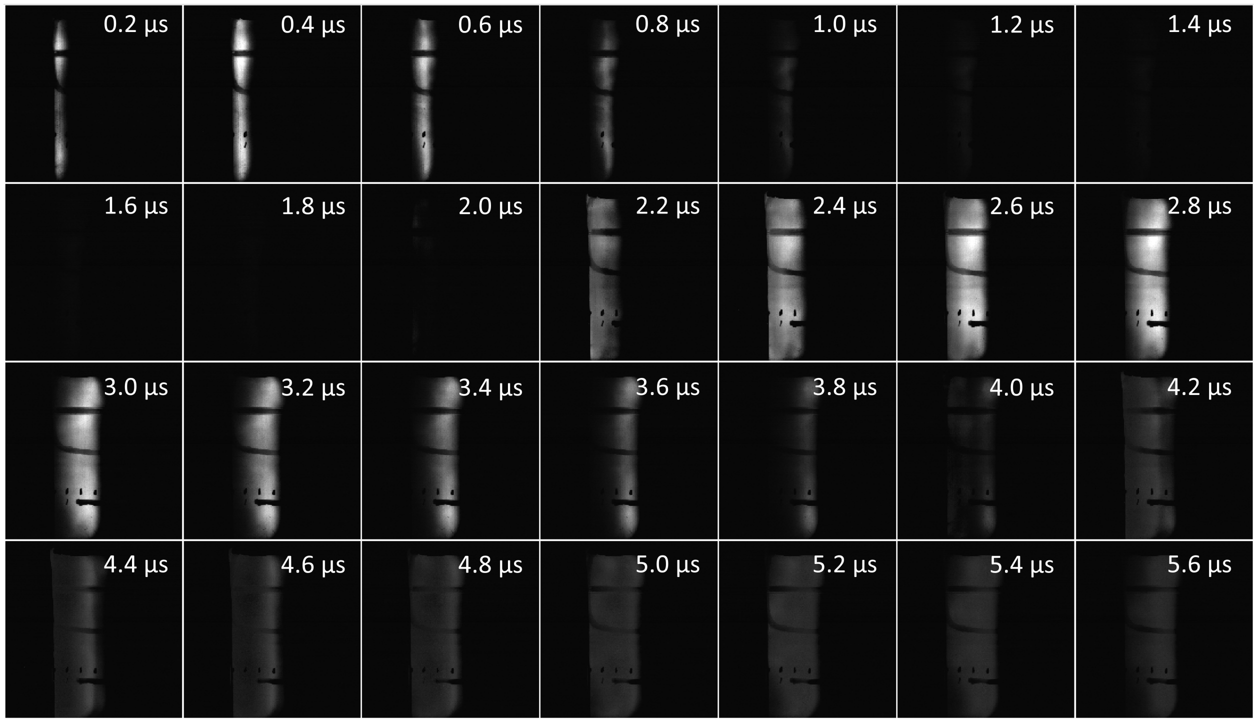

Figure B.2: Images of the plasma taken using the Kirana high-speed camera at 5,000,000 frames per second. Images taken represent an expanded increased voltage case featuring multiple plasma entities. Images are referenced to a start time of the coil circuit closing. Data is measured at the conditions described in Table 5.1.

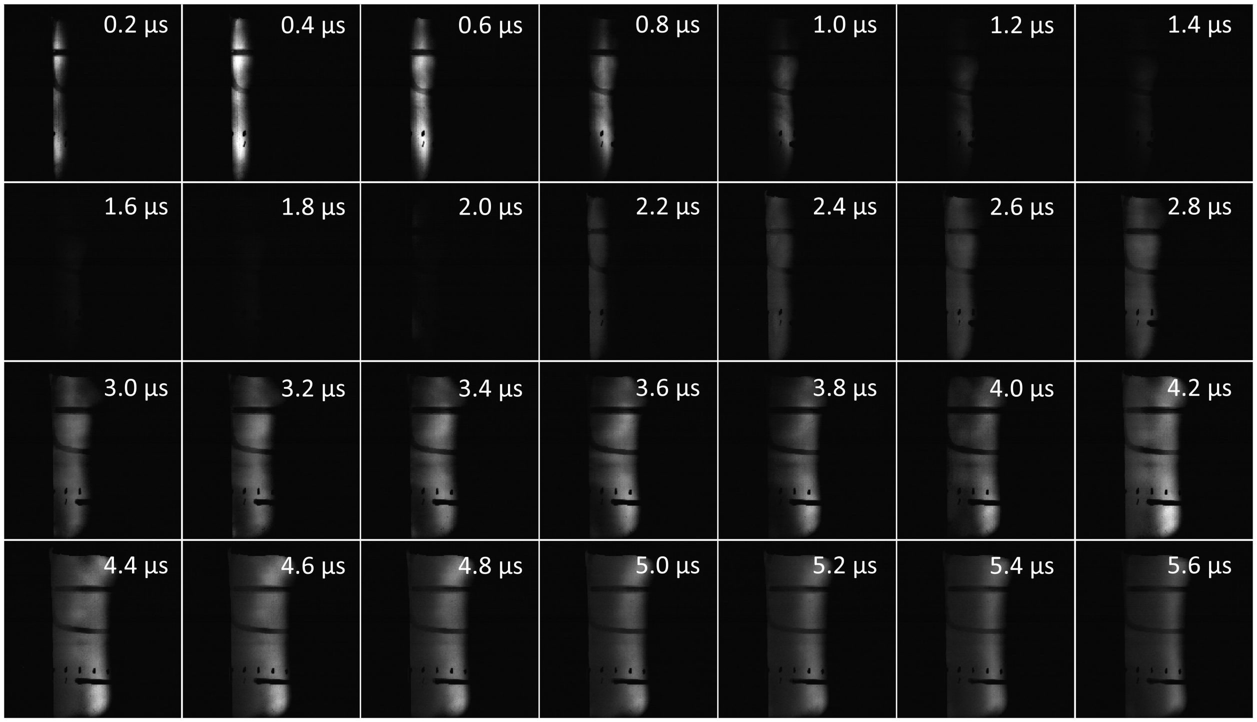

Figure B.3: Images of the plasma taken using the Kirana high-speed camera at 5,000,000 frames per second. Images taken represent an expanded increased capacitance case featuring multiple plasma entities. Images are referenced to a start time of the coil circuit closing. Data is measured at the conditions described in Table 5.1.